

# Detection of Pre-eruptive Seismic Velocity Variations at an Andesitic Volcano Using Ambient Noise Correlation on 3-Component Stations: Ubinas Volcano, Peru, 2014

R. Machacca<sup>a,b,\*</sup>, P. Lesage<sup>b</sup>, E. Larose<sup>b</sup>, P. Lacroix<sup>b</sup>, R. Anccasi<sup>a</sup>

<sup>a</sup>*Observatorio Vulcanológico del INGEMMET (Dirección de Geología Ambiental y Riesgo Geológico), Urb. Magisterial B-16, Umacollo, Arequipa, Perú*

<sup>b</sup>*Université Grenoble Alpes, Université Savoie Mont Blanc, CNRS, IRD, IFSTTAR, ISTerre, 38000 Grenoble, France*

---

## Abstract

Volcano monitoring and eruption forecasting are based on the observation and joined interpretation of several precursory phenomena. It is thus important to detect new types of precursor and to study their relationship with forthcoming eruptions. In the last years, variations of seismic velocity have been observed in some volcanoes, mainly basaltic, before eruptions. In this paper, we look for velocity variations and waveform decorrelations before the 2014 eruptive sequence of the andesitic Ubinas volcano in Peru. We compute velocity changes by using seismic ambient noise cross-correlation (between pairs of stations) and cross-components correlation (between vertical and horizontal components of single stations), as well as coda wave interferometry of seismic multiplets. With these different approaches, we show that the major explosions that occurred from 13 to 19 April were preceded by a clear velocity decrease and waveform decorrelation. The amplitude of velocity change is generally larger on single-station cross-components correlation than on two-stations cross-correlation in all the frequency ranges tested (between 0.1 and 8 Hz). We highlight an apparent anisotropy of velocity change in single-station cross-components correlation, with larger amplitudes when correlating vertical and tangential components

---

\*Corresponding author:

*Email address:* roger.machacca@gmail.com (R. Machacca)

than using vertical and radial components with respect to the crater. The  $M_w = 8.1$  Iquique earthquake on 1 April 2014 produced also a marked co-seismic velocity drop detected in a high frequency range (3-5 Hz) in both single-station cross-components correlation and cross-correlations. We locate in the horizontal plane and in depth the velocity perturbation and the structural change related with decorrelation. During the main phase of eruptive activity, the velocity decrease at low frequency (0.1-1 Hz) appears to affect the whole edifice mainly at depth of about 1 to 3 km below the surface. The structural perturbation is more concentrated on the south flank of the volcano, a zone that corresponds to an ancient collapse. We suggest that the observed velocity variations are due to the dilatation of the edifice and to microfracturation induced by magma pressurization. The structural change may be locally enhanced by a possible zone of material weakness in the southern sector. The co-seismic velocity perturbation is located mostly in the southeast flank, at depth smaller than 0.5 to 1 km, and may be related to the presence of the hydrothermal system of the volcano.

*Keywords:* Seismic velocity variation, coda wave interferometry, eruption precursor, volcano monitoring, Ubinas volcano, volcano seismology

---

## 1. Introduction

The early detection of volcanic unrest before a forthcoming eruption is one of the primary goals of volcano observatories. For that purpose, it is necessary to identify and analyze a maximum number of precursory phenomena that are the basis of eruption forecasting. The most widely used precursors are the increase of the seismic activity, the ground deformation (inflation) and the variation of gas flow and composition (Scarpa and Gasparini, 1996). However, these phenomena are not always observed before eruptions (Kato et al., 2015; Romero et al., 2016) and it is important to investigate other types of precursors.

The variations of seismic velocity in volcanic structures appear to be a promising precursory phenomena that have been recently observed on some volcanoes. Seismic velocity changes caused by large earthquakes or volcanic ac-

13 tivity have been detected first by using repeating earthquakes (Poupinet et al.,  
14 1984; Ratdomopurbo and Poupinet, 1995) or active seismic sources (Nishimura  
15 et al., 2005). However, this approach is not easily applicable for continuous  
16 monitoring because it depends on the occurrence of repeating earthquakes with  
17 similar sources. Several authors have demonstrated that the Earth’s impulse  
18 response (Green’s function) between two passive receivers can be retrieved by  
19 cross-correlating ambient seismic noise (Weaver and Lobkis, 2001; Shapiro and  
20 Campillo, 2004); Ambient Noise is a permanent vibration of the ground surface  
21 due to human activity or natural processes such as the interaction of the oceanic  
22 swell with the solid Earth. These virtual records provide the opportunity for  
23 imaging and monitoring a medium without using active seismic sources (Shapiro  
24 et al., 2005; Wegler et al., 2009; Larose et al., 2015). Furthermore, Larose et al.,  
25 (2010), Obermann et al., (2013) and Planès et al., (2014) introduced a method  
26 to locate, in the horizontal plane, spatially heterogeneous velocity or structure  
27 perturbations.

28 Brenguier et al., (2008) calculated velocity variations by comparing ambient  
29 noise cross-correlation functions obtained at different periods and evidenced ve-  
30 locity decreases prior to eruptions at Piton de la Fournaise volcano, La Réunion  
31 Island. More recently De Plaen et al., (2016) also estimated velocity reductions  
32 before eruptions of Piton de la Fournaise by using auto-correlation and correla-  
33 tion between components of a single station. Haney et al. (2015); Bennington  
34 et al. (2015; 2018) also show the application of ambient noise cross-components  
35 correlation of single stations for study seasonal and magmatic velocity variations  
36 at Okmok and Veniaminof volcanoes.

37 Temporal changes in the subsurface velocity structure during volcanic ac-  
38 tivity are likely controlled by several factors, such as stress, deformation, and  
39 migration of magmatic or hydrothermal fluids (e.g. Sens-Schönfelder et al.,  
40 2014; Donaldson et al., 2017). Up to now, velocity variations preceding volcanic  
41 eruptions have been detected only at a limited number of volcanoes such as  
42 Piton de la Fournaise (Brenguier et al., 2008; Duputel et al., 2009; Clarke et  
43 al., 2013; Obermann et al., 2013; Rivet et al., 2014; 2015; Sens-Schönfelder et

44 al., 2014; De Plaen et al., 2016), Ruapehu (Mordret et al., 2010), Miyakejima  
45 (Anggono et al., 2012), Etna (Cannata, 2012; De Plaen et al., 2019), Okmok  
46 (Bennington et al., 2015), Mt St Helens (Hotovec-Ellis et al., 2015), Merapi  
47 (Budi-Santoso and Lesage, 2016), or Kilauea (Donaldson et al., 2017), Hakone  
48 (Yukutake et al., 2016), Veniaminof (Bennington et al., 2018) or White Island  
49 (Yates et al., 2019). However, at some open systems such as Volcán de Colima,  
50 the velocity variations were almost undetectable (Lesage et al., 2014), even be-  
51 fore large eruptive events (Lesage et al., 2018). It is thus important to keep  
52 evaluating and documenting this approach on an increasing number of cases.

53 In this study, we investigate the velocity changes associated with the 2014  
54 eruptive cycle of Ubinas volcano, Peru, and with the  $M_w = 8.1$  Iquique earth-  
55 quake. We use ambient Noise Correlation Function (NCF) calculated between  
56 station pairs, Noise Cross-Correlation Function (NCCF) and Noise Single-station  
57 Cross-components correlation Functions (NSCF) calculated between different  
58 components of the same stations. Additionally, we analyze similar events (mul-  
59 tiplets) to detect pre-eruptive velocity changes in the structure of Ubinas by  
60 using also Coda Wave Interferometry (Snieder, 2006). We explore the velocity  
61 variations in several frequency bands in order to discriminate possible veloc-  
62 ity perturbations at different depths and to identify the best spectral intervals  
63 in terms of forecasting. We localize in the horizontal plane the velocity varia-  
64 tions and the structure changes associated with the main eruption, using the  
65 sensitivity of multiply scattered waves to weak changes in the medium (Ober-  
66 mann et al., 2013). Then we interpret the estimated velocity changes in relation  
67 with other observations, such as seismicity, plume elevation, satellite thermal  
68 anomalies and  $SO_2$  flux, associated with the volcanic activity.

## 69 **2. Geological setting**

### 70 *2.1. Tectonic context*

71 Southern Peru is an active tectonic zone where the Nazca plate is subducted  
72 beneath the South American plate, with a convergence rate of about 62 mm/year

73 (Villegas et al., 2016). This subduction is accompanied by a high level of seis-  
74 micity (Chlieh et al., 2011) and volcanism along an active continental margin  
75 (Figure 1a). Active stratovolcanoes are located on the Central Volcanic Zone  
76 (CVZ), a segment associated to a steeply dipping ( $25 - 30^\circ$ ) slab extending  
77 from north of Chile to southern Peru. In this part of Peru, several volcanoes are  
78 considered as potentially dangerous among others El Misti, Ubinas, Sabancaya,  
79 Ticsani, Tutupaca, Coropuna, Yucamane, Huaynaputina. The region was also  
80 the site of the largest explosive eruption in historical times within the Andes  
81 (Huaynaputina volcano; AD 1600; VEI 6; Thouret et al., 1999). Several large  
82 earthquakes ( $M_w > 7.0$ ) occurred along the subduction zone in the past decades.  
83 For instance, on 1 April 2014, a  $M_w$  8.1 interplate thrust earthquake occurred  
84 off-shore of Iquique city, Northern Chile (epicenter  $19.572^\circ$  S,  $70.908^\circ$  W,  $\sim 360$   
85 km south of Ubinas volcano, figure 1a). The global Centroid Moment Tensor  
86 (gCMT) solution indicates an almost pure double-couple faulting geometry with  
87 strike  $357^\circ$ , dip  $18^\circ$ , and rake  $109^\circ$ , at a centroid depth of 21.9 km and centroid  
88 location south of the hypocenter, (Lay et al., 2014, Duputel et al., 2015). In  
89 Arequipa and Ubinas Valley the movement was felt for more than a minute with  
90 IV Modified Mercalli Intensity.

## 91 *2.2. Ubinas volcano*

92 Ubinas volcano (Figure 1) is considered as the most active volcano of Peru  
93 (Thouret et al., 2005; Rivera et al., 2014) and is located at about  $\sim 65$  km to the  
94 East of Arequipa city. Two main periods were identified in its eruptive history.  
95 The first one, “Ubinas I”, from middle Pleistocene to  $\sim 370$  ka ago, is charac-  
96 terized by andesite and dacite lava flows that built the lower part of the edifice.  
97 The south flank of this edifice collapsed, resulting in a debris-avalanche deposit  
98 on the SE of the summit. The second one, “Ubinas II”, ( $\sim 370$  ka to present)  
99 comprises several stages. The summit cone was built by a series of andesite and  
100 dacite lava flows and pyroclastic deposits. During the last stage, between 20  
101 and 1 ka, the eruptive behavior has been dominantly explosive, and the summit  
102 caldera was formed in association with a large-scale Plinian eruption, between

103 20 and 14 ka (Figure 3a). The last Plinian eruption occurred in  $980 \pm 60$  year  
104 BP. Since then, Ubinas displays a persistent phreatic and explosive activity. In  
105 the past 550 years, 26 volcanic unrests have been reported (VEI 1 – 3), the  
106 last two eruptions occurred in 2006-2009 and 2014-2017. An average of 6 to 7  
107 eruptions per century was estimated (Rivera et al., 2014).

108

### 109 *2.3. Chronology of the 2013 – 2016 eruption*

110 The previous eruptive period of Ubinas Volcano was on 2006 – 2009. It  
111 included episodes of magma extrusion and vulcanian explosions associated to  
112 strong degassing and a large number of elevated plumes (Macedo et al., 2009;  
113 Rivera et al., 2010, 2014; Traversa et al., 2011; Inza et al., 2014; Machacca, 2012;  
114 Figure 2). In 2013, after four years of quiescence, a new eruptive activity started  
115 with nine phreatic explosions and tremor activity between September 2 and 7. In  
116 the following months, the activity came back to the normal background level. On  
117 January 2014 a new increase in seismic activity started, followed on 1 February  
118 by an increase of tremor activity that marked the beginning of magma extrusion  
119 and degassing. On 20 February, 2014, the first harmonic tremor was recorded,  
120 indicating lava extrusion in the crater (INGEMMET internal reports; Machacca  
121 et al., SGP, 2014). The lava extrusion was confirmed during a field survey on 1  
122 March by the staff of Instituto Geofísico del Perú who reported an incandescent  
123 lava body at the bottom of the crater (Figure 3c; delimited by the red dashed  
124 line). Thermal anomalies were also detected by the MIROVA hot-spot detection  
125 system (Coppola et al., 2015). This activity increased significantly until the first  
126 major explosion on 13 April.

127 Several large explosive events occurred between 13 and 19 April, 2014, and  
128 ejected blocks of fresh basaltic andesite magma,  $40 \times 40 \times 50$  cm in size, up  
129 to 2.6 km from the active crater. The volcanic plume exceeded 5 km above  
130 the crater level and a block of  $5 \times 4 \times 2$  m has been found inside the summit  
131 caldera, at 660 m from the active vent (INGEMMET internal reports). After the  
132 major explosion on 19 April, the seismic energy and explosive activity gradually

133 declined, with weak plume emissions and sporadic series of explosions (Figure  
134 2).

### 135 **3. Data and methods**

#### 136 *3.1. Seismic network and processing*

137 During the study period, January to May, 2014, the Ubinas Network of IN-  
138 GEMMET Volcano Observatory (OVI) was composed by seven seismic stations  
139 (with codes UBN01 to UBN07) distributed around the volcano (Figure 1b). The  
140 distances between stations ranged from 2 to 12 km. The stations were equipped  
141 with three-components Guralp 6TD broadband seismometers with frequency  
142 range 30s - 100 Hz and recorded with sampling frequency of 100 Hz and A/D  
143 resolution of 24 bit. Station UBN06 began to record on July 29, 2013, UBN02  
144 on 14 February 2014 for and UBN01, UBN03, UBN04, UBN05 and UBN07 on  
145 20 to 25 March. During the eruption, UBN02 and UBN06 transmitted the data  
146 via telemetry radio to the monitoring center of OVI in Arequipa-Peru.

147 The seismic activity at Ubinas volcano during the 2014 crisis presented sev-  
148 eral types of earthquake including Volcano-Tectonic (VT) events, Long-Period  
149 events (LP), Tremor, Hybrid events (HYB), Very-Long Period events (VLP)  
150 and other types (Machacca et al., 2014; Figure 13a), classification was made  
151 considering their waveforms, spectrum and spectrogram.

152 Real-time seismic amplitude measurement (RSAM; Endo and Murray, 1991)  
153 was calculated after removing manually regional earthquakes from the records,  
154 by filtering in the [0.1 – 1] and [1 – 20] Hz frequency band and using a 10 min  
155 moving window.

156 Seismic energy has been calculated using the equation formulated by Johnson  
157 and Aster (2005).

$$E(iT) = \frac{2\pi r^2 \rho c S^2}{A} \int_0^T y^2(t) d(t) \quad (1)$$

158 where  $r$  is the distance from source,  $\rho$  is the density,  $c$  is the P wave velocity,  
159  $A$  is the attenuation correction,  $S$  the seismic site response correction and  $y(t)$

160 is the particle velocity. We assumed that the source was at shallow depth below  
161 the crater,  $\rho = 2600 \text{ kgm}^{-3}$ ,  $c = 3000 \text{ ms}^{-1}$ ,  $A$  and  $S$  were fixed at 1.

### 162 *3.2. Other observations*

163 Several complementary methods were used to observe the volcanic activity at  
164 Ubinas. Deformations of the edifice were monitored by using electronic distance  
165 measurement (e.d.m.) on several lines as shown on figure 1b. Two video cameras  
166 (Simple webcam and AXIS Q1765-LE), located at 6.5 and 25 km from the active  
167 crater, which recorded one picture every 30 s. Plume elevation from mid-2013  
168 to 30 June 2014 was estimated using the nearest camera which has a maximum  
169 visibility on the crater. The thermal anomalies of Ubinas volcano were detected  
170 by MIROVA (Middle InfraRed Observations of Volcanic Activity; Coppola et  
171 al. 2015). The  $SO_2$  flux was measured with a mobile scanning DOAS during  
172 field surveys. Temperature in hot spring “Ubinas Termal” was measured every 5  
173 minutes by a data-logger and a sensor with a precision of 0.01 °C and calibrated  
174 before installation. This spring is located at 2.2 km from UBN06 seismic station  
175 and at 5.8 km from the active crater (Figure 1b).

### 176 *3.3. Calculation of seismic ambient noise correlation functions*

177 We first prepared waveforms from each component and station in one hour  
178 long segments, after removing the mean and trend. Instrumental corrections  
179 were not necessary because the same type of sensor is used at all the stations,  
180 and the instrument responses are stable over time. As a second step, we down  
181 sampled the signal to 50Hz, then we applied spectral whitening and we filtered  
182 the records in several frequency ranges (0.1 – 1 Hz, 0.3 – 1 Hz, 1 – 3 Hz, 3 – 5 Hz,  
183 5 – 8 Hz) in order to study the velocity perturbations at different depths. Then,  
184 in order to suppress high amplitude events, we performed amplitude normal-  
185 ization in the time domain. We tested three methods — one-bit normalization  
186 (Larose et al., 2004), division by the envelope (Budi-Santoso and Lesage, 2016),  
187 and amplitude clipping (Bensen et al., 2007) — and we decided to use the clip-  
188 ping method because it produced slightly smoother curves of velocity variation.

189 This method consists in clipping the amplitudes larger than 3 times the RMS  
190 value of the record, thus reducing the weight of large events while keeping all  
191 the information contained in the low-amplitude continuous signal.

192 After that we computed the noise correlation function (NCF) for each hour  
193 and averaged them over 24 hours (Wapenaar et al., 2010). For simplicity, the  
194 acronym ‘NCF’ will refer to both NCCF and NSCF. Daily NCFs calculated with  
195 less than 6 hours of data are discarded because of their low signal-to-noise ratio  
196 (SNR). We calculated NCCF for 21 pairs of vertical components and NSCF  
197 between vertical and horizontal components of all stations. The NCCF are sen-  
198 sitive to perturbations in the medium around the path between two stations and  
199 NSCF are sensitive to the medium around one station. Figure 4 displays exam-  
200 ples of daily NSCFs and NCCFs calculated over several months (correlograms).  
201 In our case, the correlation functions obtained between pairs of stations and be-  
202 tween components of single stations are approximately symmetrical and stable  
203 over time. Thus we merged the causal and acausal sides of the NCFs and we  
204 kept a section of their coda, starting after the Rayleigh waves and ending before  
205 the SNR is too low (for example for delays of 10 to 60 s; black rectangles with  
206 spaced triangles in figure 4). Finally, before compute velocity changes ( $dv/v$ ),  
207 we applied the Butterworth bandpass filters with the same previous frequency  
208 bands and the Wiener filter once to the correlograms (2-D array) for increasing  
209 the SNR and smoothing the NCFs (Hadziioannou et al., 2011, Moreau et al.,  
210 2017).

### 211 *3.4. Estimation of velocity variations*

212 Any change in velocity or structure of the propagation medium generates  
213 modifications of the Green’s functions such as variations of the travel times  
214 of direct and coda waves and changes in the waveforms. The corresponding  
215 ambient seismic noise correlations functions (NCFs) can thus be used to detect  
216 perturbations in the medium by comparing the current NCF to a reference  
217 NCF. In particular, two methods can be used to estimate the variations of  
218 waves travel times: the Stretching Method (Lobkis and Weaver, 2003) and

219 the Moving Window Cross-Spectral (MWCS) method also known as doublet  
 220 method (Poupinet et al., 1984; Clarke et al., 2011). We tested both methods,  
 221 using as reference the average NCF over the whole study period and we obtained  
 222 similar patterns of relative velocity changes  $dv/v$  (Figure 5). However in our  
 223 case, the stretching method appears to produce more stable curves of velocity  
 224 variation, i.e. with less fluctuations, and thus we decided to use this method in  
 225 the following computations.

226 The stretching method operates in the time domain and consists in stretching  
 227 or compressing the reference or the current NCF in order to maximize the cor-  
 228 relation coefficient ( $CC$ ) between the two functions in a selected delay window,  
 229 generally in the coda. More precisely, a grid-search on the stretching coefficient  
 230 is carried out and the value  $\varepsilon$  that gives the maximum of  $CC$  is assumed to  
 231 correspond to the relative velocity variation of the medium:  $\varepsilon = dt/t = -dv/v$ .  
 232 This relation stands for a homogeneous velocity change in the structure sam-  
 233 pled by the seismic waves. In the general case, the perturbation is not uniform  
 234 and  $dv/v$  should be considered as an ‘apparent’ velocity variation (AVV). The  
 235 correlation coefficient is calculated as:

$$CC(\varepsilon) = \frac{\int_{t_1}^{t_2} NCF_{c,\varepsilon}(t)NCF_r(t)dt}{\sqrt{\int_{t_1}^{t_2} (NCF_{c,\varepsilon}(t))^2 dt} \sqrt{\int_{t_1}^{t_2} (NCF_r(t))^2 dt}} \quad (2)$$

236 where  $NCF_r(t)$  and  $NCF_c(t)$  denote respectively the reference and the current  
 237 stretched noise correlation functions and  $t_1$  and  $t_2$  are the limits of the time  
 238 window used. The subscript  $\varepsilon$  stands for the stretched version of the NCF.  
 239 The uncertainty on  $dv/v$  is estimated using the theoretical formula proposed by  
 240 Weaver et al. (2011):  
 241

$$\sigma_d = \frac{\sqrt{1 - CC^2}}{2CC} \sqrt{\frac{6\sqrt{\frac{\pi}{2}}T}{\omega_c^2(t_2^3 - t_1^3)}} \quad (3)$$

242 where  $T$  is the inverse of the frequency bandwidth and  $\omega_c$  is the central fre-  
 243 quency. The same procedure is applied when using noise cross-correlation func-  
 244

245 tions calculated between pairs of station and single-station cross-components.  
246 Figure 6 displays an example of velocity change over four months, with the  
247 corresponding  $CC$  and uncertainty obtained by the stretching method using as  
248 reference the averaged NCF.

### 249 *3.5. Estimation of velocity variations without reference*

250 When the medium is affected by significant structural and velocity changes,  
251 the estimation of velocity variations may depend on the choice of the reference  
252 NCF (Sens-Schönfelder et al., 2014). In order to improve the precision and to  
253 increase the robustness of the estimation of velocity variations, we calculated  
254 the velocity variation without reference, following the formulation proposed by  
255 Brenguier et al., (2014). In this method we calculate the velocity variation  
256 between all the pairs of daily NCFs with the stretching method. Each day is  
257 thus compared to each other days, making a full 2D matrix of relative velocity  
258 variations. Then, we reconstruct the time series of velocity variation by using  
259 a Bayesian least-squares inversion (Tarantola and Valette, 1982). Significant  
260 differences are obtained in the velocity variations calculated using the stack of  
261 all daily NCFs as a reference (figure 6). For example, the amplitude of the large  
262 velocity decrease in April (-0.7 %) obtained with a fixed reference is smaller  
263 than that calculated without reference (-1.0 %). Furthermore, on May the ve-  
264 locity calculated with reference almost recovers its previous value ( $\sim 0\%$ ), while  
265 the estimation without reference stabilizes at about -0.3 %. Advantages of the  
266 technique without reference have been discussed by Brenguier et al. (2014) and  
267 Gómez-García et al. (2018). In this study, we decided to use the stretching  
268 method without reference to estimate AVV, because several stations were in-  
269 stalled at the end of March 2014, precluding the identification of stable periods  
270 that could be used as references.

### 271 *3.6. Seismic multiplets*

272 Velocity variations can also be tracked by using families of seismic events  
273 with similar waveforms called seismic multiplets (Ratdomopurbo and Poupinet,

1995; Cannata, 2012; Hotovec-Ellis et al., 2014; Budi-Santoso and Lesage, 2016).  
For our period of study, multiplets were obtained using the records of LP events  
at UBN02 station from February to April 2014. Families of similar events were  
identified by waveform cross-correlation with the GISMO toolkit (Thompson  
and Reyes, 2017). The traces were band-pass filtered in the range 0.5 to 5 Hz  
and cross-correlated over a window from 2 s before to 3 s after the picked P-wave  
arrival time. Then correlation coefficients were calculated between each pair of  
events and clusters were defined for a correlation threshold of 0.8. Finally, those  
multiplets signals are used to estimate velocity variations, similar to the steps  
described in subsection 3.4.

### 3.7. Location of velocity and de-correlation perturbations in 2D

We used the apparent velocity variations and the amplitudes of decorrela-  
tion estimated for various station pairs and delay windows in the coda of NCF  
to locate the source of these perturbations in the horizontal plane. Decorrela-  
tion (DC) corresponds to one minus the correlation coefficient (CC). For this  
purpose, a relationship between the AVV and the physical local velocity pertur-  
bations  $dv/v(x_0)$  was defined. Then the spatial distribution of velocity change  
was estimated as an inverse problem. Similar relationship between decorrela-  
tions and scattering cross-section density can be found and used. We followed an  
approach proposed by Larose et al. (2010), and Planès (2013) to carry out the  
mapping of velocity variations and structural changes in the horizontal plane.  
This procedure assumes that the coda of NCFs are mainly multiply scattered  
surface waves (Pacheco and Snieder, 2005) and it uses sensitivity kernels based  
on a solution of the radiative transfer equation (Shang and Gao, 1988; Sato,  
1993; Paasschens, 1997; Planès, 2013). Analytical developments and details on  
the inversion procedure are presented in Appendix A.

## 4. Analysis of apparent velocity variations

In the following we examine the temporal AVV estimated using NCCF be-  
tween several station pairs, NSCF between different components of single sta-

303 tions and their dependence with frequency. We computed the NCFs in several  
304 frequency bands (0.1 – 1 Hz, 0.3 – 1 Hz, 1 – 3 Hz, 3 – 5 Hz and 5 – 8 Hz) for  
305 estimating AVV at different depths bellow the crater, and then stretched them  
306 in several time windows in the coda (with delays 10 – 60 s, 8 – 60 s, 5 – 40 s, 4  
307 – 35 s and 3 – 30 s, respectively).

#### 308 *4.1. Influence of frequency band*

309 We computed the NCCF and corresponding velocity variations for the 21  
310 possible pairs of station in five frequency bands. As an example, the behavior  
311 of velocity variations calculated for pair [UBN05 – UBN06] strongly depends on  
312 the frequency considered (Figure 7a). At high frequency [1 – 3 Hz, 3 – 5 Hz  
313 and 5 – 8 Hz], a sharp velocity drop occurred during or just after the 8.1 Mw  
314 Iquique earthquake. This sudden change is not observed at low frequencies [0.1  
315 – 1 Hz and 0.3 – 1 Hz]. However, in the later spectral bands, a marked velocity  
316 decrease is detected prior and during the eruptive activity of Ubinas volcano.  
317 The velocities returned toward their previous values after the main explosions  
318 with different characteristic times. The frequency dependence of the results will  
319 be interpreted later (see section 6) with regard to the penetration depth and  
320 dispersion of surface waves.

321 We further calculated NSCF between vertical and horizontal components of  
322 single stations for several frequency bands and we estimated the corresponding  
323 AVV. The results are quite similar to those obtained from NCCF (Figure 7b). A  
324 sharp velocity drop, concomitant with the Iquique earthquake, is also observed  
325 for the three highest frequency bands. The amplitude of this velocity drop is  
326 generally larger on NSCF than on NCCF. This may result partly from differences  
327 in the volumes of the medium sampled by the diffuse waves used by the two types  
328 of correlation function. In the two low frequency bands, progressive decrease  
329 of velocity down to -0.8 % is obtained beginning mid-March, about one month  
330 before the major explosion of 19 April 2014.

331 *4.2. Velocity variations and decorrelations associated with the volcanic activity*

332 As demonstrated in the preceding section, while the velocity is strongly  
333 perturbed by the large tectonic earthquake at high frequency, clear decreases of  
334 the velocity are detected up to one month before the main eruptive activity of  
335 Ubinas volcano. Here, we focus on estimations of velocity variation in the band  
336  $[0.1 - 1 \text{ Hz}]$  using both NCCF and NSCF at several stations.

337 Figure 8a displays the velocity variations obtained for several pairs of sta-  
338 tion, indicated in figure 1b. Here, we chose station pairs for which the records  
339 are more continuous, because some stations as UBN01 and UBN03 have gaps in  
340 the data availability. All the curves present similar behavior characterized by a  
341 clear decrease before the eruption and velocity recovering after the main explo-  
342 sions. The amplitude of velocity variations depends on the station pair used,  
343 an observation that will be useful to locate the perturbations in the structure  
344 (see section 5). Figure 8b displays the variations of the  $DC$  obtained with the  
345 stretching method for the same station pairs as in figure 8a. Similarly, there  
346 are clear differences between pairs in the variations of  $DC$ . The largest velocity  
347 variation (AVV) and decorrelation (DC) prior the main eruption are obtained  
348 for pair (UBN05-UBN06). They partially recover after the eruptive period.

349 In figure 8c, we display some AVVs calculated from NSCF, using component  
350 pairs for which the AVVs are larger. A progressive velocity decrease is observed  
351 for all the stations, starting on March 18 for the southern station UBN06 where  
352 the largest variation (-0.8 %) is obtained. After one of the major explosions,  
353 on 13 April 2014, the velocity began to recover without returning to its initial  
354 values in the study period.

355 Overall, and considering various seismic station pairs and frequency bands,  
356 we observe a clear pre-eruptive velocity decrease using ambient noise correlation  
357 in all the analyzed station pairs in  $0.1 - 1 \text{ Hz}$  frequency band.

358 *4.3. Anisotropy of apparent velocity variations*

359 The velocity changes obtained from NSCF generally have different ampli-  
360 tude when calculated with Vertical-East (Z-E) and Vertical-North (Z-N) com-

361 ponents at the same station. For example, at UBN06 the velocity decrease in  
362 Z-E components is larger than for Z-N components, and at UBN04 the velocity  
363 decrease in Z-E components is smaller than for Z-N components. It appears  
364 that velocity changes are stronger when they are calculated between the vertical  
365 and the horizontal component closest to the tangential direction with respect  
366 to the crater. With this observation in mind, we computed the noise corre-  
367 lation function and velocity variations for the Vertical-Radial (Z-R) and the  
368 Vertical-Transverse (Z-T) components with respect to the crater. The results  
369 are displayed in figure 9 where it can be observed that the velocity changes are  
370 larger when using the Z-T components than the Z-R components. In some  
371 cases, no variations at all are detected using Z-R components. The error bars  
372 calculated with equation 3 are smaller than the velocity variations obtained for  
373 the Z-T components (Figure 9c). This confirms the reliability of the differences  
374 in behavior between the two component pairs.

375 Cross-correlation between Z-T and Z-R components therefore suggest an  
376 apparent anisotropy in the velocity change. In term of early warning, AVV for  
377 Z-T components seems to be the more useful combination.

#### 378 4.4. *Velocity variations calculated by using seismic multiplets*

379 We analyzed the 20 most populated families of LP events recorded at UBN02  
380 during the volcanic unrest. Two events belong to the same family if the cor-  
381 relation coeficient between them is larger or equal to 0.8. The corresponding  
382 waveforms, their spectrum and stack, as well as the number of events in each  
383 family are presented in figure 10. The spectra of most families have a dominant  
384 peak at about 3 Hz. Some of them have spectral peaks close to 1 Hz. The  
385 occurrence of those events is displayed on figure 11a. While some families (# 1,  
386 2, 3, 6, 10, 16) occurred only before the eruptive crisis, other families (# 12, 20)  
387 occurred after the main explosions. Most of the remaining families (# 4, 5, 7, 9,  
388 11, 14, 18) were active during the eruptive cycle but they spanned over periods  
389 too short to be used for velocity change detections. Finally, 5 families (# 6, 8,  
390 12, 13, 19) could be used to estimate temporal velocity variations as they are

391 relatively well spread in time. However, none of the multiplets extended over  
392 the whole study period.

393 Multiplet can be obtained by clustering repetitive earthquakes, and then  
394 used also to estimate AVV. They can be used to check the validity of AVV from  
395 noise correlations, or as additional independent inputs.

396 To estimate AVV with multiplets, the waveforms of each family were aligned  
397 on the first arrivals. To improve those times, we cross-correlated all events  
398 between -2 s before and to 3 s after their manually picked first arrival, then we  
399 corrected the times adding the delay that maximize the CC. Finally, using the  
400 first event as reference, the coda of the remaining events were stretched in the  
401 delay window [7 – 30 s] in order to maximize the correlation coefficient. When  
402 the resulting maximum of correlation was smaller than 0.5, the corresponding  
403 value of velocity variation was discarded. Figure 11b present the comparison  
404 between the velocity variations estimated with the five selected multiplets and  
405 the velocity variations obtained from NSCF. Although the values obtained with  
406 multiplets are somewhat scattered and extend over a short duration, they are  
407 consistent with the trend obtained by ambient noise. From mid-March to 10  
408 April, the results obtained with both approaches indicate a decreasing velocity,  
409 while before this period and after the main explosions, they show stable or  
410 slightly increasing velocity.

411 The AVV obtained from multiplets confirm those obtained from noise corre-  
412 lations. As a matter of fact, due to their sparse distribution in time, they also  
413 show lower time-resolved AVV than AVV observed from NCFs.

## 414 **5. Spatial localization of medium perturbations**

415 As shown earlier in the article, the estimated velocity variations present  
416 different amplitudes, depending on the station pairs used and their position  
417 with respect to the crater. For example, the velocity decreases associated to  
418 station pairs for which the direct path crosses the crater are larger than the  
419 others. Similar patterns are observed in the time series of decorrelation. These

420 observations were used to locate the perturbations of velocity and structural  
421 changes in the medium.

422 In figures 8a and 8b, we define 4 periods: the first one (21 to 27 March  
423 2014), just after the completion of the seismic network, is used as a reference  
424 (*Ref*);  $P_1$  (29 March to 01 April 2014) when the velocity began to decrease;  $P_2$   
425 (04 to 09 April 2014) when the velocity reached its minimum, prior to the main  
426 explosion; and  $P_3$  (20 to 24 April 2014) when the velocity came back to its initial  
427 values after the main explosions. Therefore, the localization of velocity change  
428 and decorrelation for the periods of interest ( $P_1$ ,  $P_2$  and  $P_3$ ) are calculated with  
429 respect to the reference (*Ref*) period. Here only the 0.1 – 1 Hz band is used.  
430 Additionally, we locate perturbations of velocity at high frequencies triggered  
431 by the Iquique earthquake. In figure 7 the  $dv/v$  shape for 1–3, 3–5 and 5–8  
432 Hz bands are quite similar, indicating a change occurring over a large range  
433 of depth. We chose the intermediate frequency (3-5 Hz) to locate the velocity  
434 variations in the horizontal plane, for two differently defined periods: *Ref2* (24  
435 to 31 March 2014) as reference and  $P_{AEQ}$  (6 to 13 April 2014) when the velocity  
436 dropped after the earthquake.

### 437 5.1. Results

438 Figure 12 displays the maps of the velocity perturbations and of the struc-  
439 tural changes for the three periods. For period  $P_1$  (Figure 12a & 12d), a weak  
440 negative variation in velocity is observed in the whole edifice, especially close to  
441 the crater, as well as a small structural change on the East flank of the volcano  
442 near station UBN02. During period  $P_2$ , a pre-eruptive velocity decrease with  
443 larger amplitude extends again over the whole edifice. The zone of maximal  
444 variation coincides with that of structural change on the south flank of the vol-  
445 cano (Figure 12b & 12e). After the main explosion on 19 April (period  $P_3$ ), the  
446 velocity returns close to the level of period  $P_1$ . However, a structural change  
447 with lower amplitude remains on the Southern and Eastern flanks (Figure 12c &  
448 12f). The restitution index (Vergely et al., 2010) is larger than one in the whole  
449 edifice (Figure 12g) which indicates that the perturbations are well recovered.

450 On the other hand, the velocity perturbation due to the Iquique earthquake is  
451 located mainly in the Southeast flank of the volcano (Figure 12h).

### 452 *5.2. Sensitivity of velocity variations to depth of perturbation*

453 In order to estimate the depth of the perturbations, we assumed that Rayleigh  
454 waves are dominant in the coda and we computed the sensitivity of their veloc-  
455 ity to velocity perturbation at depth. The corresponding sensitivity kernels are  
456 the derivative of the Rayleigh wave phase velocity with respect to the S wave  
457 velocity for various frequencies. We used a stratified velocity model (Figure  
458 13a) obtained by solving the coupled hypocenter-velocity problem for 264 local  
459 volcano-tectonic earthquakes recorded by 4 or more stations at Ubinas (Kissling,  
460 1994). In this model, the flat surface lies at 4500 m o.s.l. As expected, the depth  
461 of highest sensitivity increases as frequency decreases. Apparent velocity vari-  
462 ations calculated in frequency ranges higher than 1 Hz are mainly sensitive to  
463 perturbations at depths smaller than 0.5 to 1 km below the surface (Figure 13a).  
464 This confirms that sharp velocity decreases in the shallow layers of volcanoes  
465 can be induced by the shaking of large earthquakes (Figure 7). The effect can  
466 result from the mechanical softening of the granular volcanic material due to  
467 nonlinear elastic behavior (Johnson and Jia, 2005; Lesage et al., 2014).

468 The velocity changes at frequencies lower than 1 Hz are sensitive to per-  
469 turbations in deeper structures of the volcano (1 - 3 km). For example, the  
470 sensitivity kernel at a frequency of 0.3 Hz has large values up to 2 km below the  
471 surface and coincides with the distribution in depth of the VT seismic activity  
472 (Figure 13b). The corresponding apparent velocity are thus sensitive to pertur-  
473 bations in the seismogenic zone of Ubinas (Figure 13c) similar to that observed  
474 for events on 2009 (Inza et al., 2014).

## 475 **6. Discussion**

### 476 *6.1. Other observations*

477 Figure 14 displays measurements of seismicity, plume elevation, thermal  
478 anomalies and  $SO_2$  flux that can be compared with the estimated velocity vari-

479 ations.

480 The volcano-tectonic activity mainly occurred in February and ended in  
481 the first days of March (Figure 14a). During the whole eruptive period, the  
482 dominant seismicity was the LP activity which peaked at a rate of over 500  
483 events per day. The volcanic system generated also important activity of tremor  
484 with total duration over 10 h/day after the first explosions (Figure 14b). A  
485 significant increase of RSAM is observed in the days before the main explosions,  
486 especially in the high-frequency band (Figure 14d). It corresponds to the high  
487 level of LP, hybrid and tremor activity. After the eruption the RSAM returned  
488 to the background level. The curve of cumulative energy shows that energy was  
489 released mostly between 29 March and 13 April 2014. After the main explosion  
490 on 19 April, the energy release came back to a low level.

491 The plume elevation began to increase on 2 February 2014 and reached its  
492 maximum during the main explosion of 19 April (Figure 14e) and some plumes  
493 possibly exceeded 5 km. The coloration of the plume got darker after the first  
494 explosions of April, indicating the presence of ash.

495 The increase of volcanic radiative power (VRP) prior the eruption indicates  
496 the emplacement of magma in the crater. The maximum value was registered  
497 on 4 April 2014. The VRP remained almost constant until the main explosion  
498 on April 19 (Figure 14f).

499 The  $SO_2$  flux measured with a mobile scanning DOAS during field surveys  
500 presented a progressive increase beginning in February and up to the main  
501 explosions (Figure 14g), a behavior similar to those of thermal anomaly and  
502 plume elevation. There were not measurements between 25 March and 12 April.

503 A sudden decrease of about  $0.35\text{ }^\circ\text{C}$  of the water temperature occurred im-  
504 mediately after the 1 April 2014 Iquique earthquake (Figure 14h). This temper-  
505 ature perturbation is highly correlated with the velocity drop observed during  
506 the passing of seismic waves. It partially recovered during the study period and  
507 after five months the temperature had returned to its initial value.

508 *6.2. Summary of main results and interpretation*

509 The main finding of the present work is the clear velocity decrease down to -  
510 0.8 % obtained by NSCF, that occurred in the three weeks prior to the explosive  
511 sequence of April 2014. This velocity decrease exceeded the seasonal fluctuation  
512 of  $dv/v$  for Ubinas volcano that ranges between  $\pm 0.2\%$  (Figure 15). Such a  
513 seasonal change is consistent with observation in other volcanos such as Okmok  
514 (Haney et al., 2015; Bennington et al., 2015), Mount St. Helens (Hotovec et  
515 al., 2015), and Veniaminof (Bennington et al., 2018). The largest variations of  
516 AVVs by NSCF were obtained at the farthest stations from the crater (UBN06  
517 and UBN07). This result differs from those of most studies where the largest  
518 AVVs are observed at the closest stations to the active crater (e.g. De Plaen et  
519 al., 2016;2019; Takano et al., 2017). This could result, at least for UBN06, from  
520 its position close to the structurally weakest part of the volcano (Figure 12).  
521 The velocity decrease appeared also clearly when using NCCF on all the station  
522 pairs, suggesting a global effect in the structure. The localization of the velocity  
523 perturbations in the horizontal plane using the AVVs obtained by NCCF, sug-  
524 gests that the sources of velocity variation were distributed in the whole edifice,  
525 with a maximal amplitude close to the crater. However this spread distribution  
526 may partly result from the poor spatial resolution of the localization method  
527 which is based on the use of diffusive waves and thus depends on their mean  
528 free path. Structural perturbations were also localized using measurements of  
529 decorrelation. The maximum of perturbation was located on the southern flank  
530 which is probably a weak zone resulting from an ancient flank collapse, and  
531 where many rockfalls take place (Figure 3f).

532 The velocity variations related to the volcanic activity were obtained at fre-  
533 quencies lower than 1 Hz. The corresponding perturbations were mainly located  
534 at depths of 1 to 3 km below the surface, which corresponds to the seismogenic  
535 zone. This suggests a possible relationship between velocity decrease and seismic  
536 activity through damaging or pressurization of the medium (Lamb et al., 2017).  
537 The velocity variations estimated by Coda Wave Interferometry using the fami-  
538 lies of similar events are consistent with those detected from noise correlation in

539 the pre-eruptive period. At frequencies higher than 1 Hz, a sharp velocity drop  
540 was observed in NCFs during the large tectonic earthquake of Iquique. This  
541 perturbation affected layers shallower than 1000 m and was located mainly in  
542 the southeast flank that corresponds to a zone of poorly consolidated material  
543 where a hydrothermal system was detected by Self-Potential studies (Gonzales  
544 et al., 2014; Byrdina et al., 2013). Numerous springs are located in this flank  
545 including “Ubinas Termal”.

546 From the methodological point of view, our estimations of the apparent  
547 velocity variations were carried out without reference correlation functions.  
548 With this approach, a time series of AVV is estimated from the calculation  
549 of  $N(N - 1)/2$  velocity variations instead of  $N$  values when using a reference  
550 NCF. It can thus produce more reliable results (Brenquier et al., 2014), es-  
551 pecially when the studied time series is too short and does not include stable  
552 periods that can be used as reference or when both the velocity and the structure  
553 of the medium are perturbed and generate decorrelation of the NCFs. In this  
554 case, and unlike the usual method which uses a unique reference NCF, values  
555 of AVV can still be obtained for the daily NCFs that are well correlated with  
556 only few of the other ones.

557 We showed that interesting information can be obtained by calculating cor-  
558 relation functions between the components of single stations. From these NSCFs  
559 we could estimate velocity variations with large amplitudes in the pre-eruptive  
560 period. This confirms the results obtained for Piton de la Fournaise, La Réunion  
561 Island by De Plaen et al. (2016), at Etna volcano by De Plaen et al. (2018), at  
562 Whakaari volcano by Yates et al. (2019), at Veniaminof volcano by Bennington  
563 et al. (2018) and provides a complementary tool for detecting precursory sig-  
564 nals of impending eruptions. Moreover we demonstrated, in the case of Ubinas  
565 volcano, that the velocity decrease was much larger when using combination of  
566 vertical and tangential components, with respect to the direction of the crater,  
567 than with the vertical and radial components. To our knowledge, this is the  
568 first evidence of an anisotropic effect of velocity variation reported in a volcanic  
569 context. It may result from an anisotropy of the fractures distribution, as sug-

570 gested by the predominance of radial faults in the shallow structure (Figure 12)  
571 and/or by the largest compliance of some families of crack or by anisotropy of  
572 velocity structure as observed by Mordret et al. 2015. It may also be related to  
573 phenomena of temporal variations of seismic anisotropy due to stress changes  
574 observed on some volcanoes (Gerst et al., 2004; Bianco et al., 2006). More  
575 observations in other volcanic or geologic contexts and theoretical studies are  
576 required to validate and interpret this phenomenon.

577 The 2014 eruptive crisis of Ubinas was well observed thanks to the use of  
578 a variety of sensors and methods (Figure 14). In the following, we propose a  
579 scenario for interpreting the set of observations.

- 580 • Mid-January 2014: First observation of hybrid seismic events and pro-  
581 gressive increase of hybrid and LP activity. On 1 February, beginning of  
582 spasmodic tremor activity and small phreatic explosions. These phenom-  
583 ena may be induced by a deep magma intrusion, that interacts with the  
584 hydrothermal system of the volcano (first km below the summit crater).  
585 Hot gas with higher mobility interacts with the hydrothermal producing  
586 the small explosions and the tremor.
- 587 • 10 February: New thermal anomaly detected by MIROVA,  $SO_2$  flux in-  
588 crease. 20 February; beginning of harmonic tremor activity. These obser-  
589 vations indicate magma extrusion in the crater.
- 590 • 18 March: velocity decreases are detected on the stations in operation.
- 591 • 29 March: LP and tremor activity increases. Strong  $SO_2$  flux is measured.  
592 Velocity decrease and decorrelation are detected on all station pairs and  
593 component pairs of single station at low frequency (0.3 – 1 Hz).
- 594 • 1 April: Mw 8.1 Iquique earthquake occurs at 360 km from Ubinas. Sharp  
595 velocity drop is observed at high frequencies (1 – 3, 3 – 5 and 5 – 8  
596 Hz) on all NCFs. It probably occurs mainly in the shallow layers of the  
597 edifice. It could result from the temporal softening of poorly consolidated  
598 granular material induced by ground shaking (Johnson and Jia, 2005;

599 Lesage et al., 2014). The passing of seismic waves can also increase the  
600 rock permeability, due to the mobilization of colloidal particles, droplets  
601 or bubbles trapped in pores (Elkhoury et al., 2006; Manga et al., 2012).  
602 Meteoric water lying in this porous material could have been released and  
603 mixed to warmer thermal water producing the rapid temperature decrease  
604 at Termal Ubinas spring. The common origin of the velocity perturbation  
605 and of the spring water disturbance may explain the temporal correlation  
606 between their occurrences. The ground shaking associated with the large  
607 tectonic earthquake may have also contributed to trigger the forthcoming  
608 eruption.

- 609 • Beginning of April: Strong increase of RSAM and seismic energy release.  
610 Velocity variations reach their maximal absolute values. Tremor dura-  
611 tion still increases. Largest thermal anomaly as revealed by MIROVA,  
612 plume heights and ash contents. Estimated extrusion rate peaks at  $1.4 \pm$   
613  $0.02m^3s^{-1}$ . All these observations can be related to the raising of magma  
614 in the conduit and the progressive pressurization of the magmatic system.  
615 The pressure source could produce compressional strain in the surround-  
616 ing medium and extensional strain at shallower depth (Budi-Santoso and  
617 Lesage, 2016; Donaldson et al., 2017) and thus could induce the aperture  
618 of some crack families and rock damaging yielding to decreasing velocity.
- 619 • 13 - 19 April: Series of large explosions producing the highest and most  
620 ash-laden plumes, maximal values of  $SO_2$  flux, extrusion and destruction  
621 of domes. RSAM and energy release decrease and seismic velocity begins  
622 to recover its previous value. The large explosions opened the conduit  
623 and depressurized the system. Magma extrusion continued as observed  
624 by thermal anomaly.

## 625 7. Concluding remarks

626 Since the development of methods based on ambient noise correlation, only a  
627 few numbers of cases presenting variations of seismic velocity before an eruption

628 of andesitic volcano have been identified. In the present study, we have obtained  
629 a very clear example of velocity decrease up to three weeks before the onset of  
630 an explosive sequence at Ubinas volcano. Our results suggest that this precursor  
631 has similar behavior on andesitic and basaltic volcanoes. Estimations of velocity  
632 changes from the analysis of seismic multiplets by coda wave interferometry  
633 gave consistent results. Velocity variations with amplitude down to -0.8 % were  
634 also detected by using seismic noise correlation between vertical and horizontal  
635 components of single stations. Moreover, the amplitudes of variation are larger  
636 when using vertical and tangential components, with respect to the direction to  
637 the crater, than using vertical and radial components. This observation suggests  
638 an anisotropic effect in the response of the seismic velocity to pressurization  
639 of the volcanic structure. Similar studies on other volcanoes and geological  
640 contexts are required to determine if this behavior is common or if it is a specific  
641 feature of Ubinas volcano. Theoretical developments would also be necessary in  
642 order to understand the origin of this anisotropy.

643 Our results have also showed that precursory velocity variations can be de-  
644 tected with NSCF calculated at single stations even if they are not close to the  
645 crater. This observation, if it is corroborated by other studies and if possible  
646 local effects of weaker structure can be discarded, would be of great interest for  
647 volcano observatories that operate sparse monitoring networks.

648 The velocity variations at Ubinas volcano in 2014 are a relatively complex  
649 phenomenon because they were induced by at least two processes: the volcanic  
650 activity and the large tectonic Iquique earthquake that occurred less than two  
651 weeks before the main explosions. However we could separate the two effects  
652 thanks to their sensitivity in different frequency ranges and the good temporal  
653 resolution of ours NCCFs. While the seismic waves generated by the earthquake  
654 produced a decrease of velocity in the shallow layers of the edifice ( $< 1$  km),  
655 the velocity perturbations related with the impending eruption were located at  
656 larger depth (1 – 3 km) and distributed in the whole volcanic structure. The  
657 question of the possible coupling between the large earthquake and the vol-  
658 canic reactivation remains open. Decorrelations of the NCFs were also detected

659 prior to the eruption. They may result from structural changes centered on the  
660 southern flank of the edifice, a weak zone due to an ancient flank collapse.

661 The 2014 eruptive crisis of Ubinas volcano was observed by different types  
662 of sensors, such as seismometers, DOAS, camera, satellite IR detector. Thanks  
663 to the analysis of this set of observations, we proposed an interpretative sce-  
664 nario of the pre- and co-eruptive periods which relates the velocity variations at  
665 low frequency to the progressive pressurization of the magmatic system before  
666 the main explosions, followed by its depressurization after the opening of the  
667 magmatic conduit.

### 668 **Acknowledgments**

669 This work was partially funded by Labex OSUG@2020 grant, the Insti-  
670 tuto Geológico Minero y Metalúrgico of Perú (INGEMMET) and Institut de  
671 Recherche pour le Développement (IRD). We acknowledge B. Valette and J.  
672 Delph for helpful scientific discussions, L. Fidel, M. Rivera and B. Zavala for  
673 their support at OVI - INGEMMET, D. Ramos, P. Masias, E. Taipe, J. Marino,  
674 R. Miranda, B. Callata, M. Ortega, I. Lazarte, J. Calderon, A. Añamuro and  
675 all the OVI team for data collection and onsite instruments maintenance during  
676 eruptive crises. We thank O. Macedo, M. Alvarez, J. Acosta and inhabitants of  
677 the Ubinas Valley for field observations and photos.

678 **References**

- 679 [1] Anggono, T., Nishimura, T., Sato, H., Ueda, H., Ukawa, M., 2012. Spatio-  
680 temporal changes in seismic velocity associated with the 2000 activity of  
681 Miyakejima volcano as inferred from cross-correlation analyses of ambient  
682 noise. *J. Volcanol. Geotherm. Res.*, 247-248: 93–107.
- 683 [2] Bennington, N.L., Haney, M., De Angelis, S., Thurber, C.H. and Frey-  
684 mueller, J., 2015. Monitoring changes in seismic velocity related to an on-  
685 going rapid inflation event at Okmok volcano, Alaska. *J. Geophys. Res.*  
686 *Solid Earth*, 120: 5664–5676.
- 687 [3] Bennington, N., Haney, M., Thurber, C., Zeng, X., 2018. Inferring magma  
688 dynamics at Veniaminof volcano via application of ambient noise. *Geophys.*  
689 *Res. Lett.*, 45, 11, 650–11, 658.
- 690 [4] Bensen, G.D., Ritzwoller, M.H., Barmin, M.P., Levshin, A.L., Lin, F.,  
691 Moschetti, M.P., Shapiro, N.M., Yang, Y., 2007. Processing seismic ambi-  
692 ent noise data to obtain reliable broad-band surface wave dispersion mea-  
693 surements. *Geophys. J. Int.*, 169: 1239–1260.
- 694 [5] Bianco, F., Scarfi, L., Del Pezzo, E., Patanè, D. Shear wave splitting  
695 changes associated with the 2001 volumecanic eruption on Mt Etna. *Geo-*  
696 *phys. J. Int.* 167, 959-967.
- 697 [6] Brenguier, F., Shapiro, N.M., Campillo, M., Ferrazzini, V., Duputel, Z.,  
698 Coutant, O., Nercessian, A., 2008. Towards forecasting volcanic eruptions  
699 using seismic noise. *Nature Geoscience*, 1:126-130.
- 700 [7] Brenguier, F., Campillo, M., Takeda, T., Aoki, Y., Shapiro, N. M., Briand,  
701 X., Emoto, K., and Miyake, H., 2014. Mapping pressurized volcanic fluids  
702 from induced crustal seismic velocity drops. *Science*, 345(6192):80–82.
- 703 [8] Budi-Santoso, A., Lesage, P., 2016. Velocity variations associated with the  
704 large 2010 eruption of Merapi volcano, Java, retrieved from seismic multi-  
705 plets and ambient noise cross-correlation. *Geophys. J. Int.*, 206(1):221-240.

- 706 [9] Byrdina, S., Ramos, D., Vandemeulebrouck, J., Masias, P., Revil, A., Fini-  
707 zola, A., Gonzales Zuñiga, K., Cruz, V., Antayhua, Y., Macedo, O., 2013.  
708 Influence of the regional topography on the remote emplacement of hy-  
709 drothermal systems with examples of Ticsani and Ubinas volcanoes, South-  
710 ern Peru. *Earth Planet. Sci. Lett.* 365, 152–164.
- 711 [10] Cannata, A., 2012. Crustal changes at Mt. Etna volcano accompanying  
712 the 2002–2003 eruption as inferred from a repeating earthquake analysis.  
713 *Geophys. Res. Lett.*, 39: L18311.
- 714 [11] Chlieh, M., Perfettini, H., Tavera, H., Avouac, J.-P., Remy, D., Nocquet,  
715 J.-M., Rolandone, F., Bondoux, F., Gabalda, G., Bonvalot S., 2011. Inter-  
716 seismic coupling and seismic potential along the Central Andes subduction  
717 zone, *J. Geophys. Res.*, 116: B12405.
- 718 [12] Clarke, D., Zaccarelli, L., Shapiro, N.M., Brenguier, F. 2011. Assessment of  
719 resolution and accuracy of the Moving Window Cross Spectral technique for  
720 monitoring crustal temporal variations using ambient seismic noise. *Geo-  
721 physical Journal International*, 186: 867–882.
- 722 [13] Clarke, D., Brenguier, F., Froger, J.L., Shapiro, N.M., Peltier, A., Stau-  
723 dacher, T., 2013. Timing of a large volcanic flank movement at Piton de la  
724 Fournaise Volcano using noise-based seismic monitoring and ground defor-  
725 mation measurements *Geophys. J. Int.*, 195(2): 1132–1140.
- 726 [14] Coppola, D., Macedo, O., Ramos, D., Finizola, A., Delle Donne, D., Del  
727 Carpio, J., White, R.A., McCausland, W., Centeno, R., Rivera, M., Apaza,  
728 F., Ccallata, B., Chilo, W., Cigolini, C., Laiolo, M., Lazarte, I., Machacca,  
729 R., Masias, P., Ortega, M., Puma, N. and Taïpe, E., 2015. Magma extru-  
730 sion during the Ubinas 2013–2014 eruptive crisis based on satellite thermal  
731 imaging (MIROVA) and ground-based monitoring. *J. Volcanol. Geotherm.  
732 Res.*, 302: 199-210.
- 733 [15] De Plaen, RSM., Cannata, A., Cannavo, F., Caudron, C., Lecocq, T., Fran-  
734 cis, O., 2019. Temporal Changes of Seismic Velocity Caused by Volcanic

- 735 Activity at Mt. Etna Revealed by the Autocorrelation of Ambient Seismic  
736 Noise. *Front. Earth Sci.* 6:251.
- 737 [16] De Plaen, R.S.M., Lecocq, T., Caudron, C., Ferrazzini, V., Francis, O.,  
738 2016. Single-station monitoring of volcanoes using seismic ambient noise.  
739 *Geophys. Res. Lett.*, 43: 8511–8518.
- 740 [17] Donaldson, C., Caudron, C., Green, R.G., Thelen, W., White, R.S., 2017.  
741 Relative seismic velocity variations correlate with deformation at Kilauea  
742 volcano. *Science Advances*, 3(6): e1700219.
- 743 [18] Duputel, Z., Ferrazzini, V., Brenguier, F., Shapiro, N.M., Campillo, M.,  
744 Nercessian, A., 2009. Real time monitoring of relative velocity changes us-  
745 ing ambient seismic noise at the Piton de la Fournaise volcano (La Réunion)  
746 from January 2006 to June 2007. *J. Volcanol. Geotherm. Res.*, 184(1-2):  
747 164–173.
- 748 [19] Duputel, Z., Jiang, J., Jolivet, R., Simons, M., Rivera, L., Ampuero, J.P.,  
749 Riel, B., Owen, S.E., Moore, A.W., Samsonov, S.V., Ortega-Culaciati,  
750 F., Minson, S.E., 2015. The Iquique earthquake sequence of April 2014:  
751 Bayesian modeling accounting for prediction uncertainty. *Geophys. Res.*  
752 *Lett.*, 42, 7949–7957.
- 753 [20] Elkhoury, J.E., Brodsky, E.E., Agnew, D.C., 2006. Seismic Waves Increase  
754 Permeability. *Nature*, 441(1):135–138.
- 755 [21] Endo, E.T., Murray, T., 1991. Real-time seismic amplitude measurement  
756 (RSAM): a volcano monitoring and prediction tool. *Bull. Volcanol.*, 53:  
757 533–545.
- 758 [22] Froment, B., 2011. Utilisation du bruit sismique ambiant dans le suivi  
759 temporel de structures géologiques. PhD Thesis, Université de Grenoble.
- 760 [23] Gerst, A., Savage, M. K., 2004. Seismic anisotropy beneath Ruapehu vol-  
761 cano: a possible eruption forecasting tool. *Science* 306, 1543-1547.

- 762 [24] Gómez-García, C., Brenguier, F., Boué, P., Shapiro, N.M., Droznin, D.V.,  
763 Droznina, S.Ya., Senyukov, S.L., Gordeev, E.I., 2018. Retrieving robust  
764 noise-based seismic velocity changes from sparse data sets: synthetic tests  
765 and application to Klyuchevskoy volcanic group (Kamchatka). *Geophys. J.*  
766 *Int.*, 214(2):1218–1236.
- 767 [25] Gonzales, K., Finizola, A., Lénat, J.F., Macedo, O., Ramos, D., Thouret,  
768 J.C., Fournier, N., Cruz, V., Pistre, K., 2014. Asymmetrical structure,  
769 hydrothermal system and edifice stability: the case of Ubinas volcano, Peru,  
770 revealed by geophysical surveys. *J. Volcanol. Geotherm. Res.* 276, 132–144.
- 771 [26] Hadziioannou, C., Larose, E., Baig, A., Roux, P., Campillo, M., 2011.  
772 Improving temporal resolution in ambient noise monitoring of seismic wave  
773 speed. *J. Geophys. Res.: Solid Earth*, 116(B07304).
- 774 [27] Haney, M. M., Hotovec-Ellis, A. J., Bennington, N. L., De Angelis, S.,  
775 Thurber, C., 2015. Tracking changes in volcanic systems with seismic in-  
776 terferometry. *Encyclopedia of Earthquake Engineering*, 3767-3786.
- 777 [28] Hotovec-Ellis, A.J., Gomberg, J., Vidale, J.E., Creager, K.C., 2014. A  
778 continuous record of intereruption velocity change at Mount St. Helens  
779 from coda wave interferometry. *J. Geophys. Res.*, 119: 2199–2214.
- 780 [29] Hotovec-Ellis, A.J., Vidale, J.E., Gomberg, J., Thelen, W., Moran,  
781 S.C., 2015. Changes in seismic velocity during the first 14months of the  
782 2004–2008 eruption of Mount St. Helens, Washington. *J. Geophys. Res.*,  
783 120: 6226–6240.
- 784 [30] IGP Report, 2013. Catálogos Sismovolcánicos Ubinas 2013. URL:  
785 [https://ovs.igp.gob.pe/sites/ovs.igp.gob.pe/files/pdf/  
786 Investigacion/catalogos/Ubinas/catalogo\\_ubinas\\_2013.pdf](https://ovs.igp.gob.pe/sites/ovs.igp.gob.pe/files/pdf/Investigacion/catalogos/Ubinas/catalogo_ubinas_2013.pdf). Ac-  
787 cessed October 2018.
- 788 [31] IGP Report, 2014. Actividad del volcán Ubinas. Reporte N° 14-

- 789 2014. URL: [https://ovs.igp.gob.pe/sites/ovs.igp.gob.pe/files/](https://ovs.igp.gob.pe/sites/ovs.igp.gob.pe/files/pdf/Ubinas/2014/reporte_ubinas_201414.pdf)  
790 [pdf/Ubinas/2014/reporte\\_ubinas\\_201414.pdf](https://ovs.igp.gob.pe/sites/ovs.igp.gob.pe/files/pdf/Ubinas/2014/reporte_ubinas_201414.pdf). Accessed October 2018.
- 791 [32] INGEMMET Report, 2014. Reporte de Monitoreo del volcán Ubinas. Re-  
792 porte N° UB14-01. URL: [http://ovi.ingemmet.gob.pe/?page\\_id=971](http://ovi.ingemmet.gob.pe/?page_id=971).  
793 Accessed October 2018.
- 794 [33] Inza, L.A., Métaxian, J.P., Mars, J., Bean, C.J., O'Brien, G.S., Macedo,  
795 O., Zandomeneghi, D., 2014. Analysis of dynamics of vulcanian activity  
796 of Ubinas volcano, using multicomponent seismic antennas. *J. Volcanol.*  
797 *Geotherm. Res.*, 270: 35-52.
- 798 [34] Johnson, J., Aster, R., 2005. Relative partitioning of acoustic and seismic  
799 energy during Strombolian eruptions. *J. Volcanol. Geotherm. Res.* 148, 334–  
800 354.
- 801 [35] Johnson, P.A., Jia, X., 2005. Nonlinear dynamics, granular media and dy-  
802 namic earthquake triggering. *Nature*, 437: 871-874.
- 803 [36] Kato, A., Terakawa, T., Yamanaka, Y., Maeda, Y., Horikawa, S., Mat-  
804 suhiro, K., Okuda, T., 2015. Preparatory and precursory processes leading  
805 up to the 2014 phreatic eruption of Mount Ontake, Japan. *Earth, Planets*  
806 *and Space* 67:111.
- 807 [37] Kissling, E., Ellsworth, W.L., Eberhart-Phillips, D., Kradolfer, U., 1994.  
808 Initial reference models in local earthquake tomography. *J. Geophys. Res.*,  
809 99: 19635–19646.
- 810 [38] Lamb, O. D., De Angelis, S., Wall, R. J., Lamur, A., Varley, N. R., Reyes-  
811 Dávila, G., et al. (2017). Seismic and experimental insights into eruption  
812 precursors at Volcán de Colima. *Geophys. Res. Lett.* 44, 6092–6100.
- 813 [39] Larose, E., Derode, A., Campillo, M., Fink, M., 2004. Imaging from one-  
814 bit correlations of wideband diffuse wave fields. *J. Applied Physics*, 95(12):  
815 8393–8399.

- 816 [40] Larose, E., Planes, T., Rossetto, V., Margerin, L., 2010. Locating a small  
817 change in a multiple scattering environment. *Applied Physics Lett.*, 96(20):  
818 110.
- 819 [41] Larose, E., Carrière, S., Voisin, C., Bottelin, P., Baillet, L., Guéguen, P.,  
820 Walter, F., Jongmans, D., Guillier, B., Garambois, S., Gimbert, F., Massey,  
821 C., 2015. Environmental Seismology: What Can We Learn on Earth Surface  
822 Processes with Ambient Noise. *Journal of Applied Geophysics*, 116, 62–74.
- 823 [42] Lay, T., Yue, H., Brodsky, E.E., An, C., 2014. The 1 April 2014 Iquique,  
824 Chile, Mw 8.1 earthquake rupture sequence, *Geophys. Res. Lett.*, 41, 3818–  
825 –3825.
- 826 [43] Lesage, P., Reyes-Dávila, G.A., Arámbula-Mendoza, R., 2014. Large tec-  
827 tonic earthquakes induce sharp temporary decreases in seismic velocity in  
828 Volcán de Colima, Mexico. *J. Geophys. Res.*, 119(5): 4360–4376.
- 829 [44] Lesage, P., Carrara, A., Pinel, V., Arámbula-Mendoza, R., 2018. Absence  
830 of detectable precursory deformation and velocity variation before the large  
831 dome collapse of July 2015 at Volcán de Colima, Mexico. *Frontiers in Earth*  
832 *Science* (in press).
- 833 [45] Lobkis, O.I., Weaver, R.L., 2003. Coda-wave interferometry in finite solids:  
834 Recovery of P-to-S conversion rates in an elastodynamic billiard. *Phys.*  
835 *Rev. Lett.*, 90(25): 254302.
- 836 [46] Macedo, O., Métaxian, J., Taïpe, E., Ramos, D., Inza, L.A., 2009. Seismic-  
837 ity associated with the 2006 – 2008 eruption, Ubinas volcano. In: Bean,  
838 C.J., Braiden, A.K., Lokmer, I., Martini, F., O’Brien, G.S. (Eds.), *The*  
839 *VOLUME Project*, 1:262–270.
- 840 [47] Machacca, R., 2012. Evaluación de eventos sísmicos de largo periodo (LP)  
841 como precursores en las explosiones del volcán Ubinas, 2006-2009. *Bach.*  
842 *Thesis*, Universidad Nacional de San Agustín de Arequipa.

- 843 [48] Machacca, R., Lesage, P., Paxi, R., Ortega, M., Rivera, M., Ccallata,  
844 B., Taïpe, E. and Ramos, D., 2014. Detección de ascenso de magma y  
845 evolución del proceso eruptivo del volcán Ubinas de 2014, observadas con  
846 datos sísmicos. *Boletín de la Sociedad Geológica del Perú*, 109: 29-33.
- 847 [49] Manga, M., Beresnev, I., Brodsky, E.E., Elkhoury, J.E., Elsworth, D.,  
848 Ingebritsen, S.E., Mays, D.C. and Wang, C.-Y., 2012. Changes in perme-  
849 ability caused by transient stresses: Field observations, experiments, and  
850 mechanisms. *Rev. Geophysics*, 50: RG2004.
- 851 [50] Mordret, A., Jolly, A.D., Duputel, Z., Fournier, N., 2010. Monitoring of  
852 phreatic eruptions using interferometry on retrieved cross-correlation func-  
853 tion from ambient seismic noise: Results from Mt. Ruapehu, New Zealand.  
854 *J. Volcanol. Geoth. Res.*, 191, 46 -- 59.
- 855 [51] Mordret, A., Rivet, D., Landès, M., Shapiro, N., 2015. Three-dimensional  
856 shear velocity anisotropic model of Piton de la Fournaise Volcano (La  
857 Réunion Island) from ambient seismic noise. *J. Geophys. Res.*, 120: 406–  
858 427.
- 859 [52] Moreau, L., Stehly, L., Boué, P., Lu, Y., Larose, E., Campillo, M. 2017.  
860 Improving ambient noise correlation functions with an SVD-based Wiener  
861 filter. *Geophys. J. Int.*, 211:418–426.
- 862 [53] Nishimura, T., Tanaka, S., Yamawaki, T., Yamamoto, H., Sano, T., Sato,  
863 M., Nakahara, H., Uchida, N., Hori, S., Sato, H., 2005. Temporal changes in  
864 seismic velocity of the crust around Iwate volcano, Japan, as inferred from  
865 analyses of repeated active seismic experiment data from 1998 to 2003.  
866 *Earth Planets Space*, 57:491–505.
- 867 [54] Obermann, A., Planès, T., Larose, E. and Campillo, M., 2013. Imaging  
868 preruptive and coeruptive structural and mechanical changes of a volcano  
869 with ambient seismic noise. *J. Geophys. Res.*, 118(12): 6285-6294.

- 870 [55] Paasschens, J., 1997. Solution of the time-dependent boltzmann equation.  
871 Physical Review E, 56(1): 1135.
- 872 [56] Pacheco, C., Snieder, R., 2005. Time-lapse travel time change of multiple  
873 scattered acoustic waves. J. Acoust. Soc. Am., 118(3): 1300–1310.
- 874 [57] Planès, T., 2013. Imagerie de changements locaux en régime de diffusion  
875 multiple. Ph.D. Thesis, Université de Grenoble.
- 876 [58] Planès, T., Larose, E., Margerin, L., Rossetto, V., Sens-Schönfelder, C.,  
877 2014. Decorrelation and phase-shift of coda waves induced by local changes:  
878 multiple scattering approach and numerical validation. Waves in Random  
879 and Complex Media, 24(2): 99–125.
- 880 [59] Poupinet, G., Ellsworth, W.L. and Fréchet, J., 1984. Monitoring velocity  
881 variations in the crust using earthquake doublets: an application to the  
882 Calaveras fault, California. J. Geophys. Res., 89:5719–5731.
- 883 [60] Ratdomopurbo, A., Poupinet, G., 1995. Monitoring a temporal change of  
884 seismic velocity in a volcano: application to the 1992 eruption of Mt. Merapi  
885 (Indonesia). Geophys. Res. Lett., 22(7): 775–778.
- 886 [61] Rivera, M., Thouret, J.C., Mariño, J., Berolatti, R., Fuentes, J., 2010.  
887 Characteristics and management of the 2006 –2008 volcanic crisis at the  
888 Ubinas volcano (Peru). J. Volcanol. Geotherm. Res. 198, 19–34.
- 889 [62] Rivera, M., Thouret, J.C., Samaniego, P., Le Pennec, J.L., 2014. The  
890 2006–2009 activity of the Ubinas volcano (Peru): Petrology of the 2006  
891 eruptive products and insights into genesis of andesite magmas, magma  
892 recharge and plumbing system. J. Volcanol. Geotherm. Res, 270:122–141.
- 893 [63] Rivet, D., Brenguier, F., Clarke, D., Shapiro, N., Peltier, A., 2014. Long-  
894 term dynamics of Piton de la Fournaise volcano from 13 years of seismic  
895 velocity change measurements and GPS observations. J. Geophys. Res.,  
896 119: 7654–7666.

- 897 [64] Rivet, D., Brenguier, F., Cappa, F., 2015. Improved detection of preerup-  
898 tive seismic velocity drops at the Piton de La Fournaise volcano. *Geophys.*  
899 *Res. Lett.*, 42(15): 6332–6339.
- 900 [65] Romero, J.E., Morgavi, D., Arzilli, F., Daga, R., Caselli, A., Reckziegel, F.,  
901 Viramonte, J., Diaz-Alvarado, J., Polacci, M., Burton, M., Perugini, D.,  
902 2016. Eruption dynamics of the 22-23 April 2015 Calbuco Volcano (South-  
903 ern Chile): Analyses of tephra fall deposits. *J. Volcanol. Geotherm. Res.*  
904 317:15-29.
- 905 [66] Rossetto, V., Margerin, L., Planes, T., Larose, E., 2011. Locating a weak  
906 change using diffuse waves: Theoretical approach and inversion procedure.  
907 *J. Applied Physics*, 109(1): 034903.
- 908 [67] Sato, H., 1993. Energy transportation in one- and two-dimensional scat-  
909 tering media: analytic solutions of the multiple isotropic scattering model.  
910 *Geophys. J. Int.*, 112: 141-146.
- 911 [68] Scarpa, R., Gasparini, P., 1996. A review of volcano geophysics and volcano-  
912 monitoring methods. In *Monitoring and Mitigation of Volcano Hazards*.  
913 Springer-Verlag, Berlin, Heidelberg, New York, 3–22.
- 914 [69] Sens-Schönfelder, C., Pomponi, E., Peltier, A., 2014. Dynamics of Piton de  
915 la Fournaise volcano observed by passive image interferometry with multi-  
916 ple references. *J. Volcanol. Geotherm. Res.*, 276: 32–45.
- 917 [70] Shang, T., Gao, L., 1988. Transportation theory of multiple scattering and  
918 its application to seismic coda waves of impulsive source. *Sci. Sin.*, 31:1503–  
919 1514.
- 920 [71] Shapiro, N.M., Campillo, M., 2004. Emergence of broadband Rayleigh  
921 waves from correlations of the ambient seismic noise. *Geophys. Res. Lett.*,  
922 31: L07614.

- 923 [72] Shapiro, N., Campillo, M., Stehly, L., and Ritzwoller, M., 2005. High  
924 resolution surface-wave tomography from ambient seismic noise. *Science*,  
925 307:615–618.
- 926 [73] Snieder, R., 2006. The theory of coda wave interferometry. *Pure Appl.*  
927 *Geophys.*, 163(2): 455-473.
- 928 [74] Takano, T., Nishimura, T., Nakahara, H., 2017. Seismic velocity changes  
929 concentrated at the shallow structure as inferred from correlation analy-  
930 ses of ambient noise during volcano deformation at Izu-Oshima, Japan. *J.*  
931 *Geophys. Res. Solid Earth*, 122:6721–6736.
- 932 [75] Tarantola, A., Valette, B., 1982. Generalized nonlinear inverse problems  
933 solved using the least squares criterion. *Rev. Geophys. Space Phys.*, 28:  
934 219–232.
- 935 [76] Thompson, G., Reyes, C., 2017. GISMO - a seismic data analysis toolbox  
936 for MATLAB [software package], [http://geoscience-community-codes.](http://geoscience-community-codes.github.io/GISMO/)  
937 [github.io/GISMO/](http://geoscience-community-codes.github.io/GISMO/). Accessed October 2017.
- 938 [77] Thouret, J.C., Davila, J., Eissen, J.P., 1999. Largest explosive eruption in  
939 historical times in the Andes at Huaynaputina volcano, A.D. 1600, southern  
940 Peru. *Geology*, vol. 27(5):435–438.
- 941 [78] Thouret, J.C., Rivera, M., Worner, G., Gerbe, M.C., Finizola, A., Fornari,  
942 M., Gonzales, K., 2005. Ubinas: the evolution of the historically most active  
943 volcano in southern Peru. *Bull. Volcanol.* 67, 557–589.
- 944 [79] Traversa, P., Lengliné, O., Macedo, O., Métaxian, J.P., Grasso, J., Inza,  
945 A., Taipei, E., 2011. Short term forecasting of explosions at Ubinas volcano  
946 Peru. *J. Geophys. Res.* 116, B11301.
- 947 [80] Vergely, J.L., Valette, B., Lallement, R., Raimond, S., 2010. Spatial distri-  
948 bution of interstellar dust in the Sun’s vicinity - Comparison with neutral  
949 sodium-bearing gas. *Astronomy & Astrophysics*, 518: A31.

- 950 [81] Villegas-Lanza, J. C., Chlieh, M., Cavalié, O., Tavera, H., Baby, P., Chire-  
951 Chira, J., Nocquet, J.M., 2016. Active tectonics of Peru: Heterogeneous  
952 interseismic coupling along the Nazca megathrust, rigid motion of the Pe-  
953 ruvian Sliver, and Subandean shortening accommodation, *J. Geophys. Res.*  
954 *Solid Earth*, 121, 7371—7394.
- 955 [82] Wapenaar, K., Slob, E., Snieder, R., Curtis, A., 2010, Tutorial on seismic  
956 interferometry. Part 2: Underlying theory and new advances, *Geophysics*,  
957 75(5), 75,A211–75,A227.
- 958 [83] Weaver, R.L., Lobkis, O.I., 2001. Ultrasonics without a source: Ther-  
959 mal fluctuation correlations at MHz frequencies. *Phys. Rev. Lett.*, 87(13):  
960 134301.
- 961 [84] Weaver, R.L., Hadziioannou, C., Larose, E., Campillo, M., 2011. On the  
962 precision of noise correlation interferometry. *Geophys. J. Int.*, 185(3):1384–  
963 1392.
- 964 [85] Wegler, U., Nakahara, H., Sens-Schoönfelder, C., Korn, M., and Shiomi,  
965 K., 2009. Sudden drop of seismic velocity after the 2004 mw 6.6 mid-niigata  
966 earthquake, japan, observed with passive image interferometry. *J. Geophys.*  
967 *Res.*, 114(B6).
- 968 [86] Yates, A. S., Savage, M. K., Jolly, A. D., Caudron, C., Hamling, I. J.,  
969 2019. Volcanic, coseismic, and seasonal changes detected at White Island  
970 (Whakaari) volcano, New Zealand, using seismic ambient noise. *Geophys.*  
971 *Res. Lett.*, 46, 99–108.
- 972 [87] Yukutake, Y., Ueno, T., Miyaoka, K., 2016. Determination of temporal  
973 changes in seismic velocity caused by volcanic activity in and around hakone  
974 volcano, central japan, using ambient seismic noise records. *Prog. in Earth*  
975 *and Planet. Sci.* (2016) 3:29.

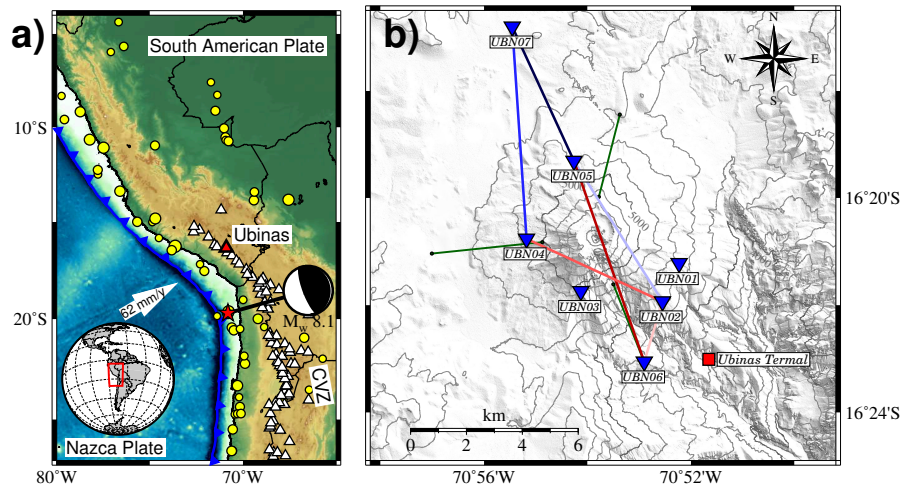


Figure 1: a) Map of the Central Volcanic Zone of southern Peru. White triangles show potentially active volcanoes. Red triangle indicates the location of Ubinas Volcano. Yellow circles are the epicenters of earthquake with magnitude larger than 7 Mw (1900-2018). The red star shows the location of the 2014 Iquique earthquake (8.1 Mw) with its focal mechanism. The blue line in the ocean is the location of the subduction trench. b) Map of Ubinas Seismic Network deployed during 2014. Inverted blue triangles: location of seismic stations. Red square: position of thermometer in spring water “Ubinas Termal”. The color lines correspond to the station pairs discussed in section 4.2. Electronic distance measurements were carried out along the green lines in 2014.

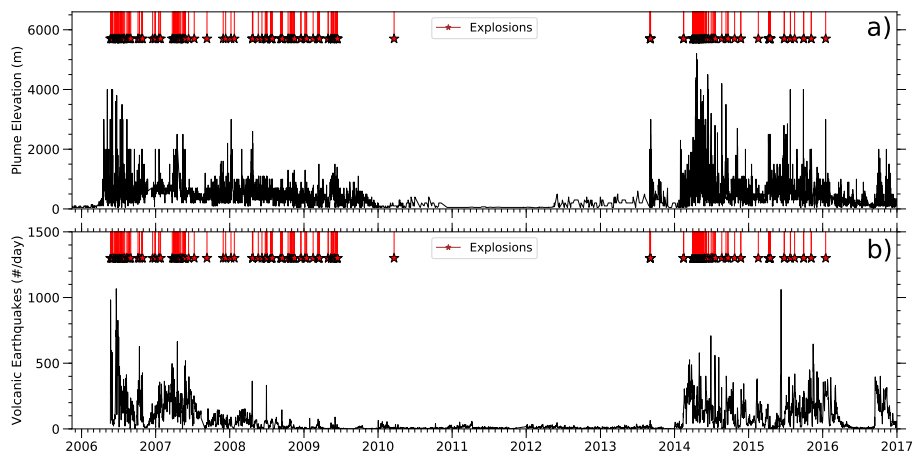


Figure 2: a) Plume elevation above crater level of Ubinas volcano recorded in the last 10 years. b) Seismic activity (sources: INGEMMET Report, 2014; IGP Report, 2013; Machacca, 2012).

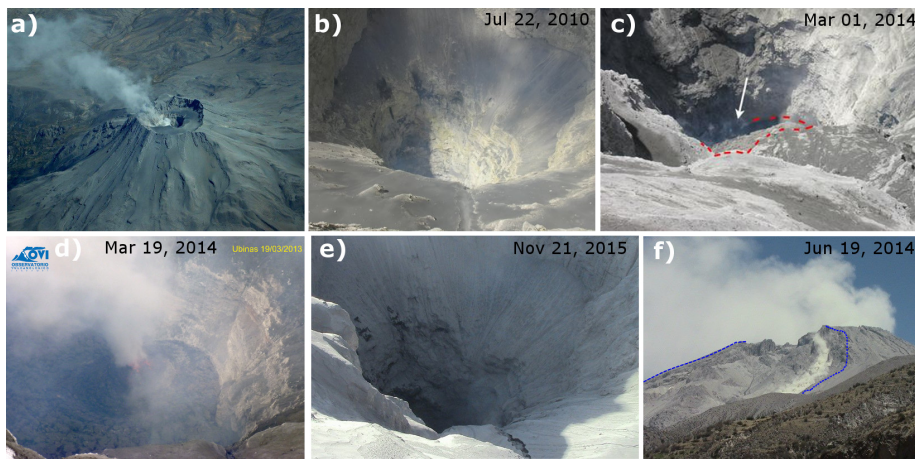


Figure 3: a) Aerial view of Ubinas volcano taken from the Northeast displaying the caldera, the active crater and fumaroles. Pictures of the active vent of Ubinas volcano on b) 2010, c) 1 March 2014, d) 19 March 2014, e) 13 June 2015. f) Rock fall during an eruption on the south flank; the old collapse scarp is indicated by blue dashed lines. Photos are from <http://lechaudrondevulcain.com> (a), R. Machacca (b), IGP Report, 2014[31] (c), J. Acosta (d), E. Alvarez (e,f).

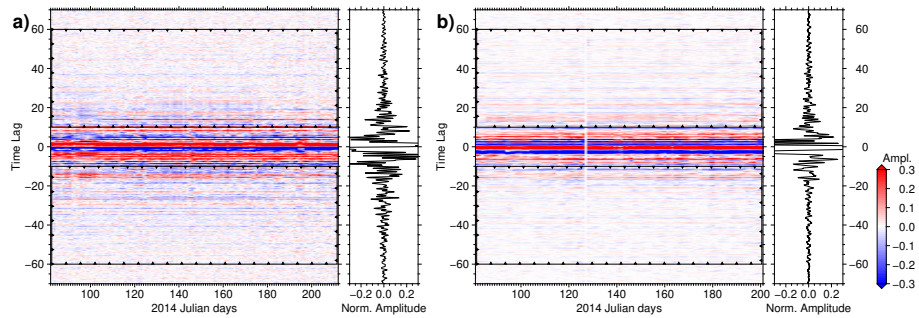


Figure 4: Daily cross-correlation functions calculated in the band  $[0.1 - 1 \text{ Hz}]$ . a) Noise Single-station Cross-components correlation Functions (NSCF) between Z and E components of UBN07 station. b) Noise Cross-correlation Functions (NCCF) of vertical components between UBN02 and UBN05. The respective waveforms correspond to the mean NCF. For this figure, we clipped the normalized amplitude from  $\pm 0.3$  for better visualization of the coda.

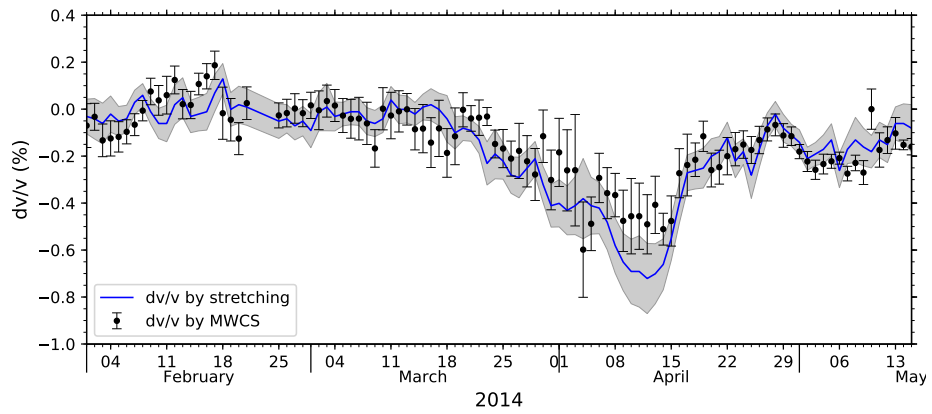


Figure 5: Comparison of the velocity changes  $dv/v$  calculated by the stretching and the MWCS methods with their respective uncertainties. The example corresponds to the single-station cross-components of Z and E components at UBN06 station [0.1-1Hz].

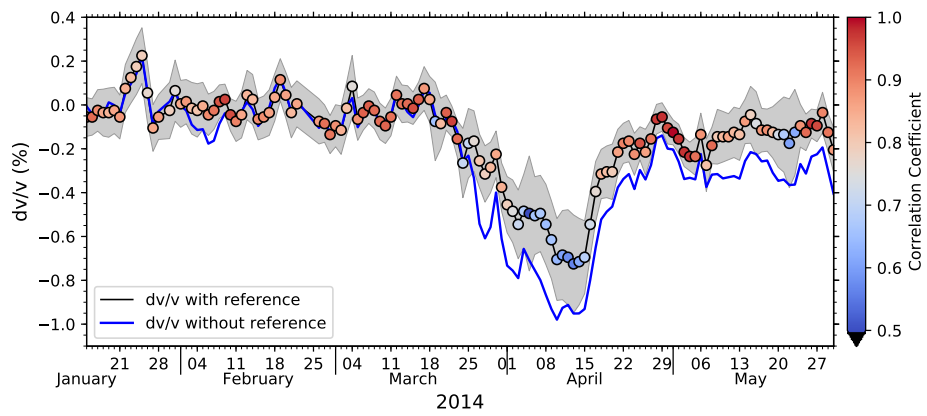


Figure 6: Comparison of the velocity changes  $dv/v$  calculated with respect to a reference NCF (black line with uncertainties represented by grey zone and correlation coefficients  $CC$  by color code) and calculated without reference (Blue line). The example corresponds to the single-station cross-components between Z and E components of station UBN06 [0.3 – 1 Hz].

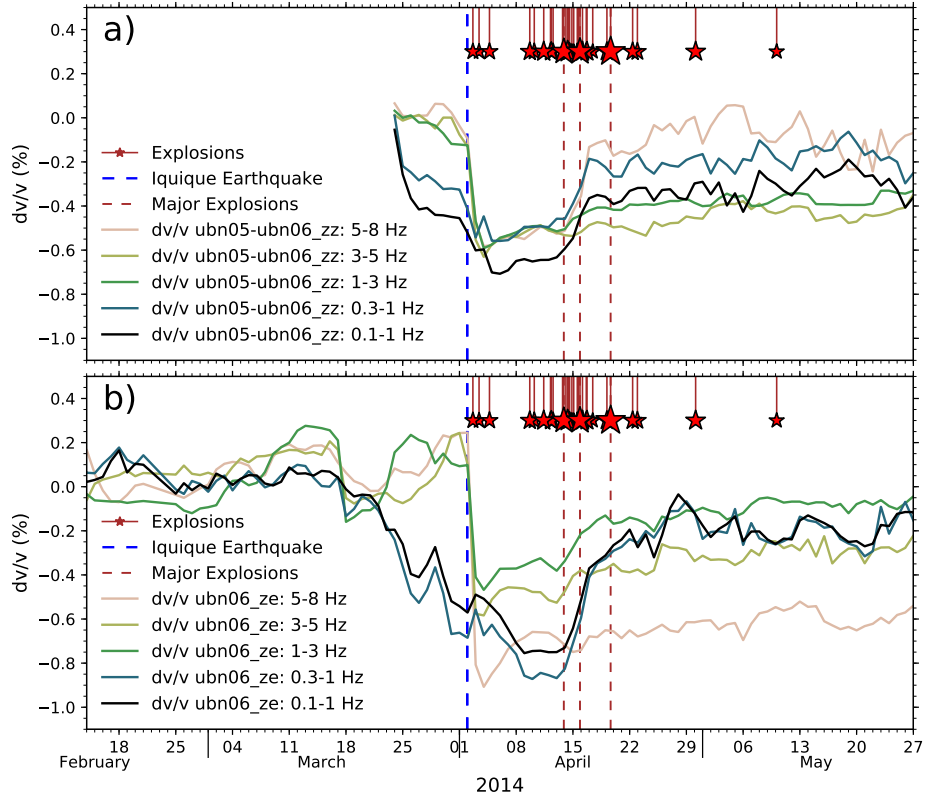


Figure 7: a) Apparent velocity variations calculated from cross-correlation functions between vertical components of UBN05 and UBN06 in five frequency bands (see legend). b) Apparent velocity variations calculated from single-station cross-components between the vertical and east components of UBN06. Vertical dashed blue and red lines indicate the occurrence of Iquique earthquake and of the major explosions, respectively. The star sizes correspond to the energy of main explosions.

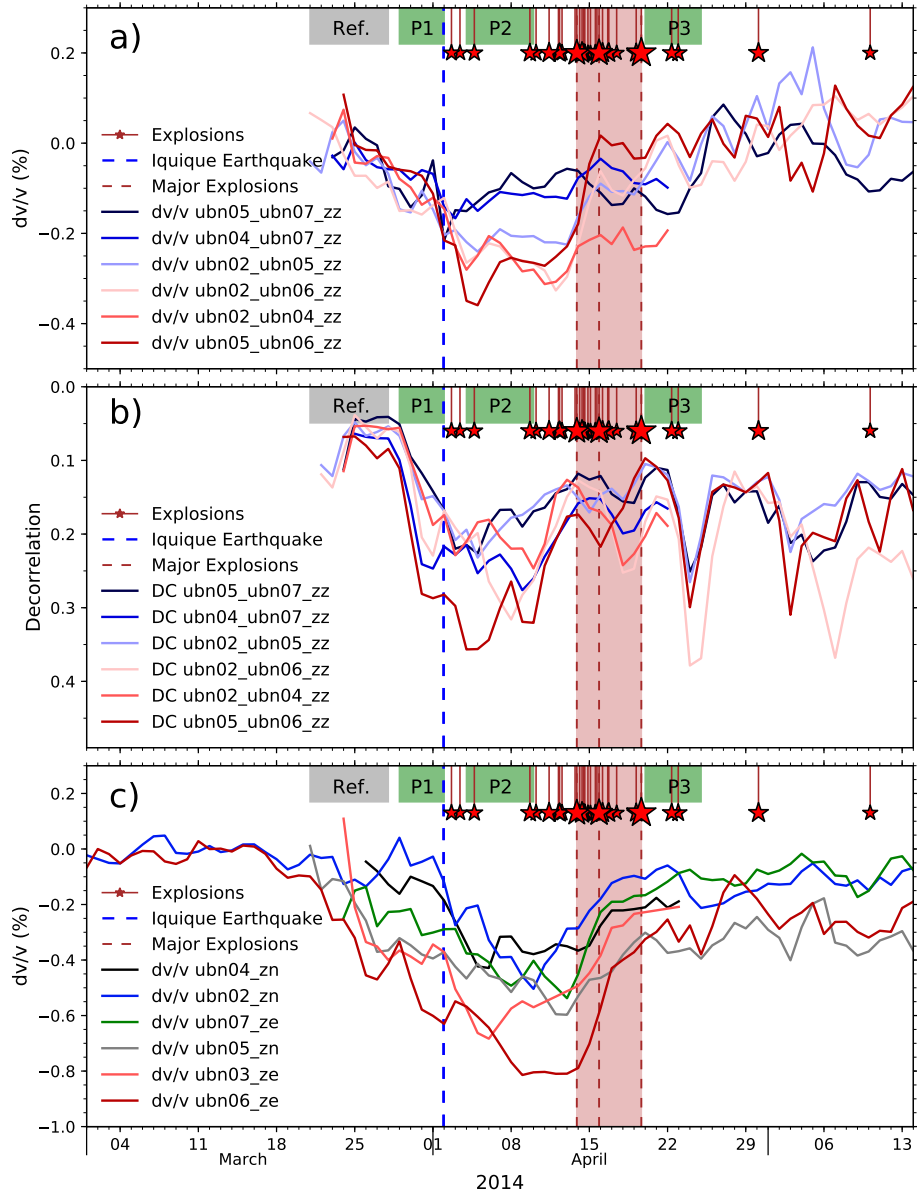


Figure 8: a) Apparent velocity variations AVV calculated from NCCF of vertical components for the pairs of station displayed in Figure 1b. Same colors are used to plot paths between stations and corresponding AVVs. b) Corresponding time series of the decorrelation ( $DC$ ). c) AVVs obtained from NSCF between vertical and horizontal components at several seismic stations. In all cases the  $dv/v$  and  $DC$  are computed for frequency range  $0.1 - 1$  Hz and delay windows  $10 - 60$  s in the coda. The  $Ref.$  and  $P_i$  boxes represent periods used for localization in 2D of velocity and decorrelation changes discussed in section 5. The red shaded zone corresponds to the main eruptive period. 44

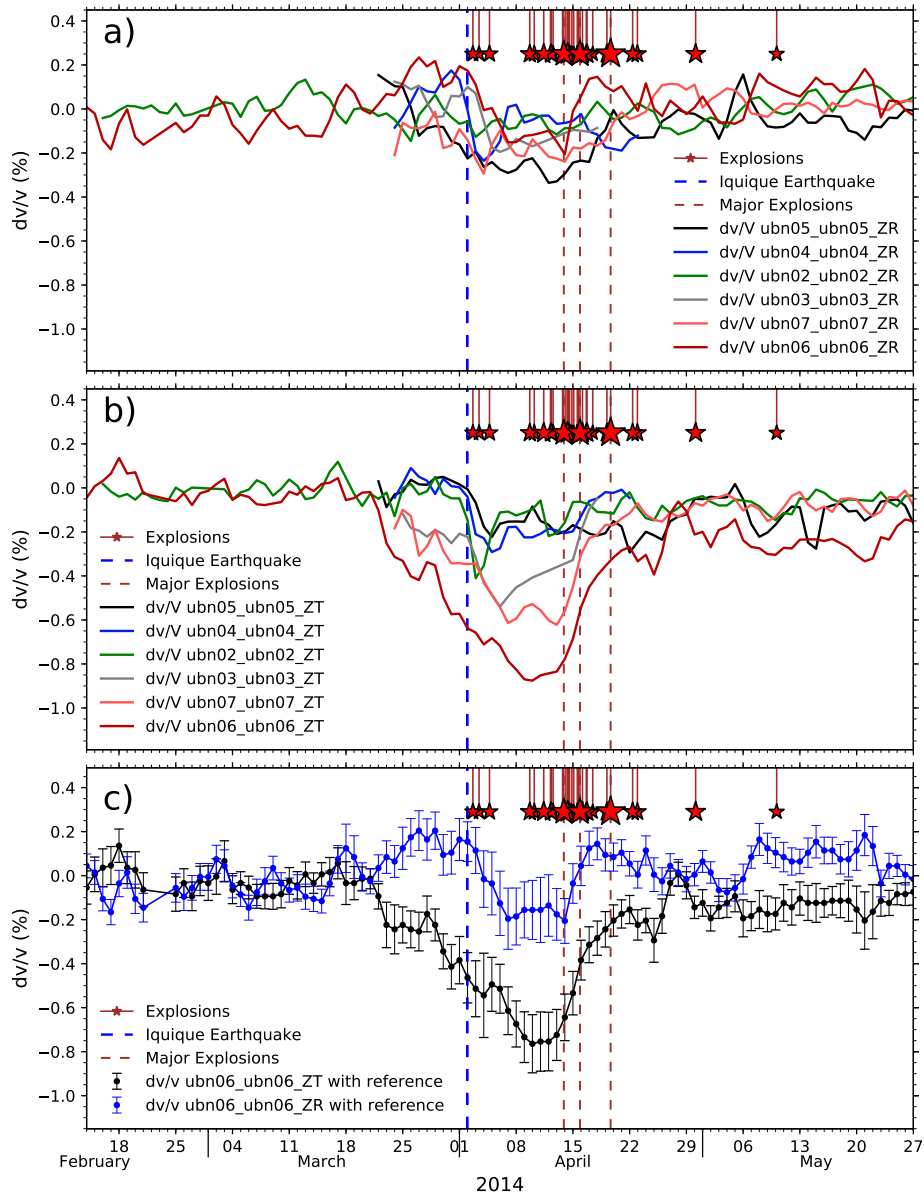


Figure 9: AVV calculated from single-station cross-components between a) Vertical and Radial components and b) Vertical and Transverse components. c) AVV obtained with reference for Z-T and Z-R components combination for station UBN06. Radial and Transverse components are with respect to the directions of the crater from each station. In all cases  $dv/v$  was computed in the range 0.1 – 1 Hz and delay window 10 – 60 s in coda.

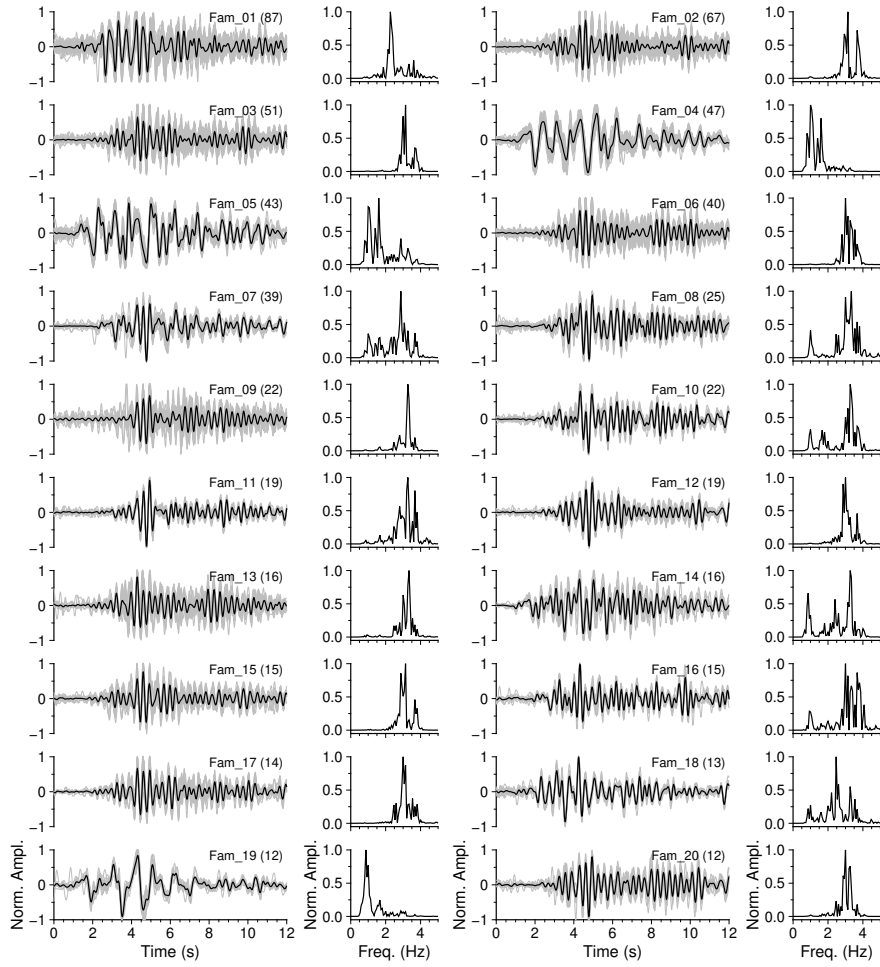


Figure 10: Twenty most populated seismic multiplets. For each cluster, the event waveforms recorded on the vertical component of UBN02 station and filtered between 0.5 and 5 Hz are plotted in grey together with their stack in black. The numbers of event in each family are indicated in parentheses. The Fourier spectra of the stacked traces are also displayed alongside.

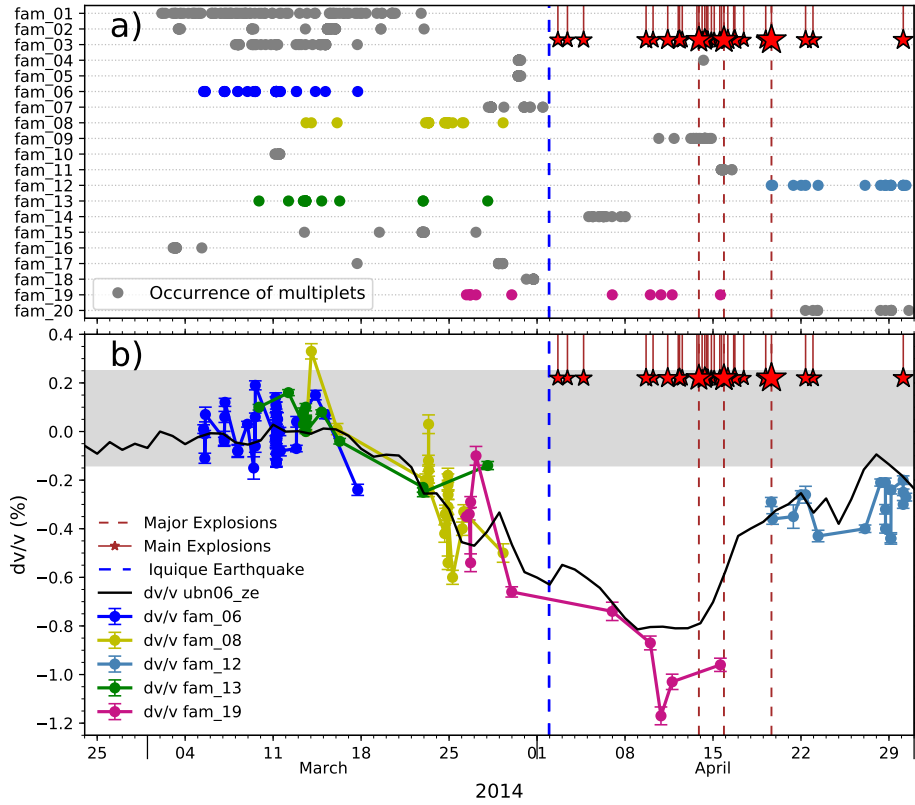


Figure 11: a) Occurrence of the LP events that belong to the main 20 families; in gray, families that have not been used to estimate  $dv/v$ . b) Velocity variations estimated by NSCF (UBN06 Z–E, black line) and multiplets with corresponding uncertainties. The width of the horizontal gray zone represents the amplitude of  $dv/v$  fluctuations obtained from NSCF before the eruption. The AVVs of families 12 and 19 were shifted to align their first value with the corresponding AVV obtained from NSCF.

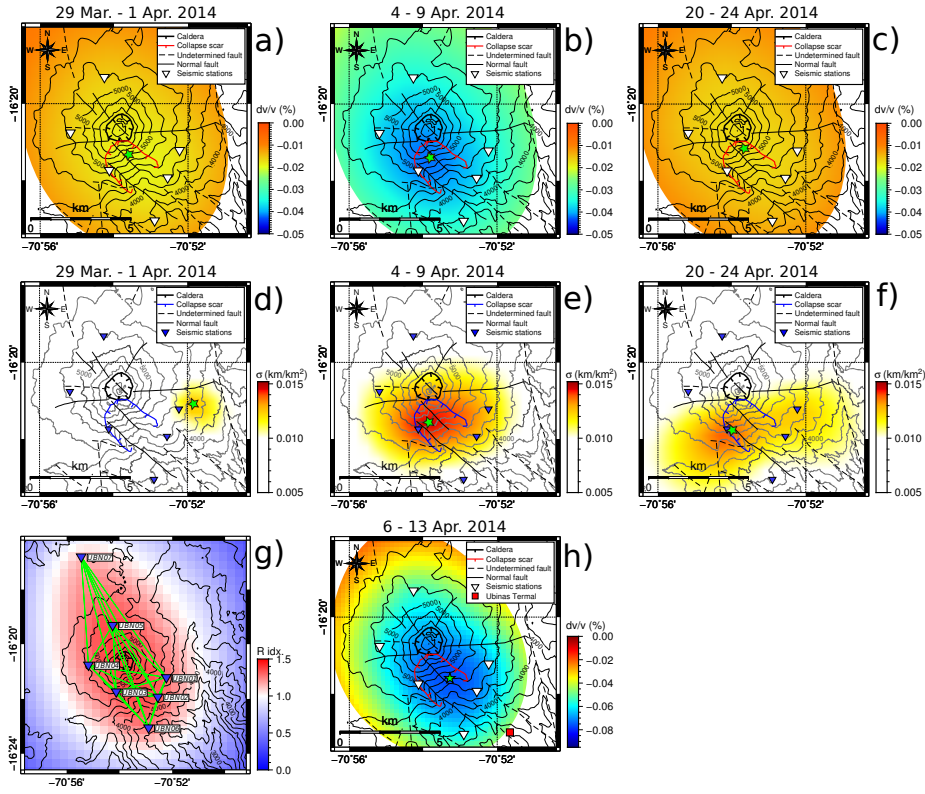


Figure 12: Maps of velocity variations (first row) and scattering cross-section density (second row) for periods  $P_1$  (a, d),  $P_2$  (b, e) and  $P_3$  (c, f) for 0.1 – 1 Hz, respectively. The maps display also the topography and the main craters and faults. The position of the maximum values of velocity variation and scattering cross-section density is indicated by green stars. g) Map of corresponding restitution index, with green lines showing station pairs. The velocity changes are plotted only for pixels where restitution index are  $\geq 1$ . h) Maps of velocity variations after the Iquique earthquake for 3 – 5 Hz and period  $P_{AEQ}$ .

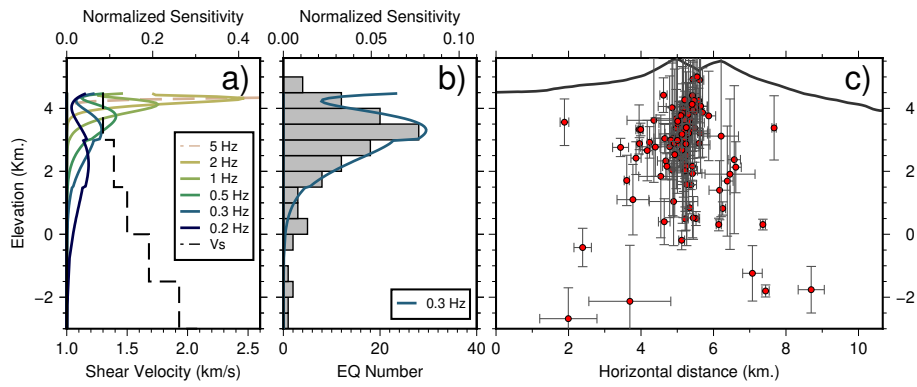


Figure 13: a) Sensitivity kernels of Rayleigh wave phase velocities to shear wave velocity for several frequencies used in this study. b) Histogram of VTs depths and sensitivity kernel of Rayleigh wave velocity for frequency of 0.3 Hz. c) Source locations of VT events for the period 26 March to 5 December 2014.

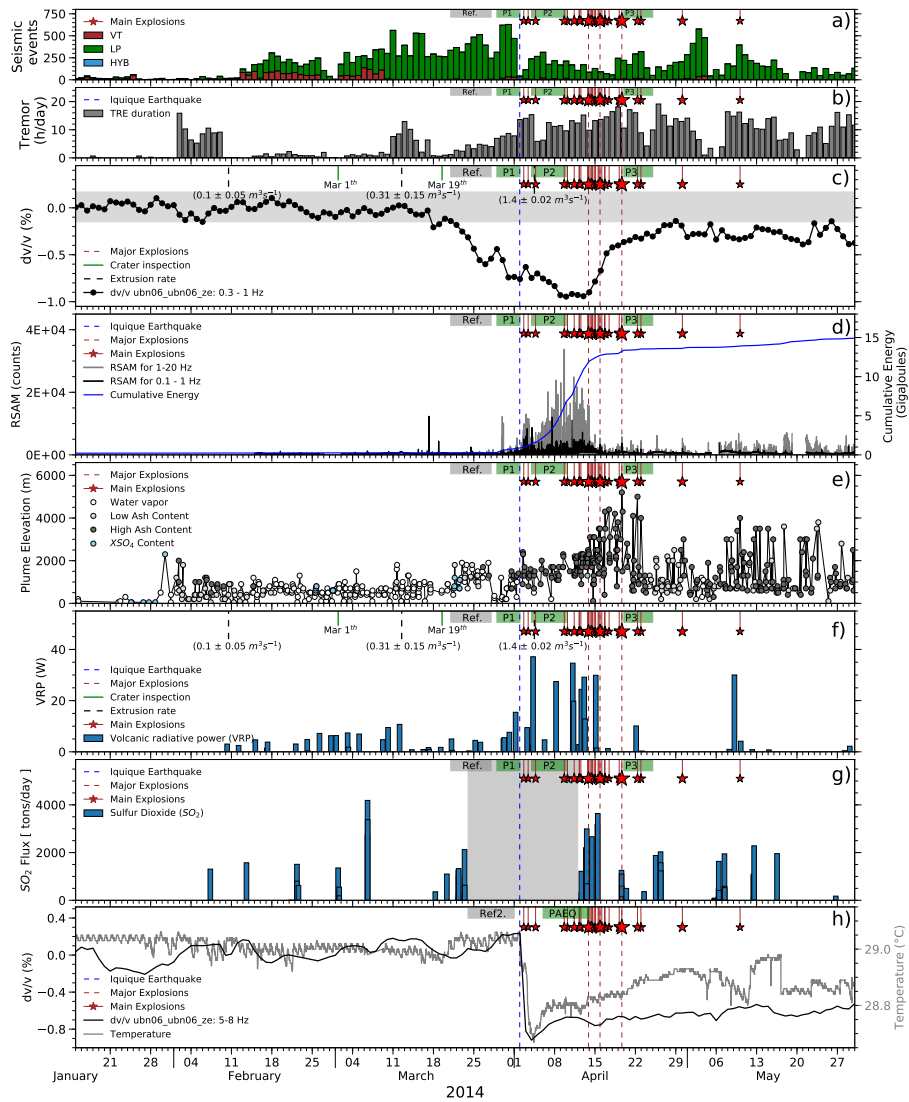


Figure 14: a) Daily count of seismic events recorded at UBN02 station. b) Duration of tremor activity. c) Velocity variations obtained by single-station cross-components between Z and E at UBN06. Estimations of extrusion rate are indicated at 3 dates (data from Copola et al., 2014[14]). d) RSAM calculated at station UBN02 in 0.1 – 1 Hz and 1 – 20 Hz frequency bands and cumulative seismic energy. e) Plume elevation with respective ash content. f) Thermal anomaly measured by Volcanic Radiative Power (VRP). g)  $\text{SO}_2$  flux determined from mobile scanning DOAS measurements. Shaded area indicated period with no measurements. h) Temperature of spring water “Ubinas Termal” (gray line) and apparent velocity variation in the 5 – 8 Hz range (dark line).

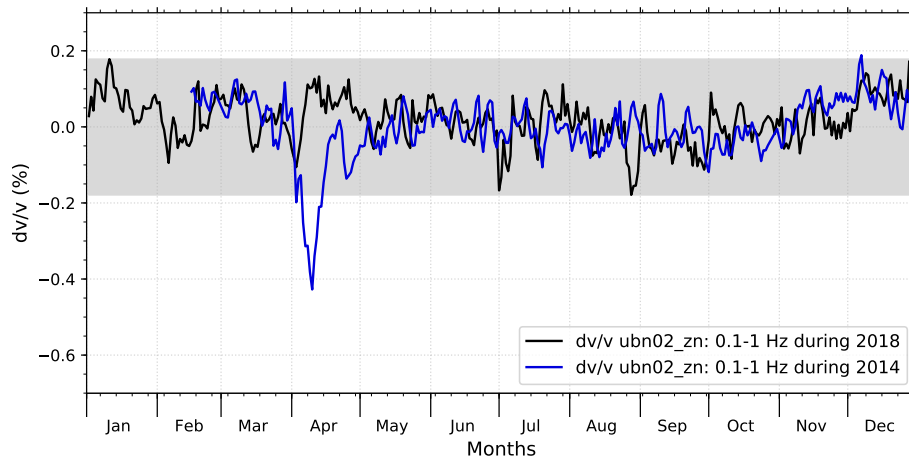


Figure 15: Comparison of  $dv/v$  obtained during a period of eruptive quiescence (year 2018, black line) with  $dv/v$  calculated for 2014 (blue line). The velocity variations associated with the eruptive crisis in April 2014 are clearly larger than the seasonal fluctuations (grey shaded area).

976 **Appendix A. Localization of velocity and structural changes**

977 *Appendix A.1. Sensitivity kernels*

978 Apparent velocity variations  $\delta v/v(t)_{app}$  estimated between station pairs are  
 979 related to the distribution of velocity perturbations  $\delta v/v(x_0)$  in the medium  $S$   
 980 by:

$$\frac{\delta v}{v}(t)_{app} = \frac{1}{t} \int_S K(s_1, s_2, x_0, t) \frac{\delta v}{v}(x_0) dS(x_0) \quad (\text{A.1})$$

981 where  $t$  is the travel time,  $s_1$  and  $s_2$  are the positions of the stations,  $x_0$  is  
 982 the location of the perturbations, and  $K$  is a sensitivity kernel introduced by  
 983 Pacheco and Snieder, (2005):

$$K(s_1, s_2, x_0, t) = \frac{\int_0^t p(s_1, x_0, u) p(x_0, s_2, t - u) du}{p(s_1, s_2, t)} \quad (\text{A.2})$$

984 The sensitivity kernel is a statistical measure of the time spent in each part of  
 985 the region under test.  $p(s_1, s_2, t)$  is the probability that the wave has traveled  
 986 from  $s_1$  to  $s_2$  during time  $t$ , which can be approximated by the intensity of the  
 987 wavefield from  $s_1$  to  $s_2$  at time  $t$ . Since surface waves are the dominant wave  
 988 type, we use the analytic two-dimensional solution of the radiative transfer for  
 989 isotropic scattering for the intensity propagator (Obermann et al., 2013):

$$p(r, t) = \frac{\exp(-ct/\ell)}{2\pi r} \delta(ct-r) + \frac{1}{2\pi \ell ct} \left(1 - \frac{r^2}{c^2 t^2}\right)^{-1/2} \exp\left(\frac{\sqrt{c^2 t^2 - r^2} - ct}{\ell}\right) \Theta(ct-r) \quad (\text{A.3})$$

990

991 where  $\ell$  is the scattering mean free path,  $\ell = \ell^*$  for isotropic scattering,  $\ell^*$  is  
 992 the transport mean free path  $\ell^* = 1/(1 - \langle \cos(\theta) \rangle)$ , where  $\theta$  is the angle between  
 993 the vector of the incident wave and the vector of the scattered wave,  $\langle \cos(\theta) \rangle$   
 994 is the anisotropy of diffusion and the brackets denote averaging over all solid  
 995 angles.  $r$  is the distance between source and receiver,  $c$  is the wave velocity, and  
 996  $\Theta$  is the Heaviside (or step) function. The first term of Equation A.3 describes  
 997 the coherent part of the intensity that decreases exponentially with the distance  
 998 relative to the transport mean free path. The second term describes the diffusion

999 intensity. Note that the diffusion solution is reached when  $t \gg r/c$ . An example  
 1000 of the sensitivity kernel is displays in Figure A.1.

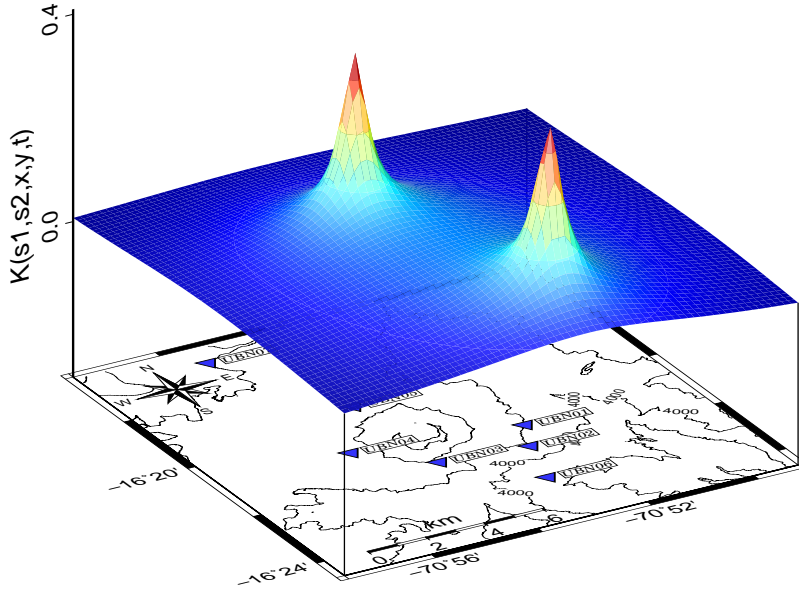


Figure A.1: Sensitivity kernel for [UBN05 - UBN06] station pair. The two peaks are located at the station positions.

1001 For the present work, we took  $c = 1.38 \text{ km/s}$  and we choose a value of mean  
 1002 free path  $\ell = 5 \text{ km}$ , as reported by Rossetto et al., (2011), who demonstrated  
 1003 that this location method is not very sensitive to the value of the mean free path.

1004

#### 1005 *Appendix A.2. Inverse problem*

1006 We follow the procedure described by Froment (2011), Obermann et al.  
 1007 (2013), and Lesage et al. (2014). Equation A.1 can be rewritten as:

$$d = Gm \tag{A.4}$$

1008 where  $d$  is the data vector, the components of which are the measured apparent  
 1009 velocity variations between two dates,  $G$  is the matrix of the sensitivity kernels  
 1010 weighted by elementary surface over time  $t$  in the coda  $G = \frac{\Delta S}{t} K$  and  $m$  is the

1011 model vector of the velocity perturbations  $\delta v/v(x_0)$  for each cell:

1012  $d = \varepsilon$ ,  $G = \frac{\Delta S}{t}K$  and  $m = \delta v/v$

1013 Because the problem is linear, we can use a formulation of least square inverse  
1014 method proposed by Tarantola and Valette (1982):

1015

$$m = m_0 + C_m G^t (G C_m G^t + C_d)^{-1} (d - G m_0) \quad (\text{A.5})$$

1016

1017 where  $m_0$  is the initial model (a zero vector) and  $C_d$  is the diagonal covariance  
1018 matrix of the data.  $C_m$  is the covariance matrix for the model which is intro-  
1019 duced in order to produce smooth models:

1020

$$C_m(i, j) = \left( \sigma_m \frac{\lambda_0}{\lambda} \right)^2 \exp \left( - \frac{d(i, j)}{\lambda} \right) \quad (\text{A.6})$$

1021 where  $d(i, j)$  is the distance between two cells  $i$  and  $j$ ,  $\lambda$  is the correlation length,  
1022  $\lambda_0$  is the cell length, and  $\sigma_m$  is an a priori standard deviation of the model. We  
1023 used values of  $\lambda = 2$  km,  $\lambda_0 = 0.5$  km and  $\sigma_m = 0.02$ . The resolution matrix  $R$   
1024 is given by:

$$R = C_m G^t (G C_m G^t + C_d)^{-1} G \quad (\text{A.7})$$

1025 The sum of the elements of row  $j$  of the matrix is the restitution index of the  
1026  $j^{\text{th}}$  cell of the model (Vergely et al., 2010). Values close to one indicate good  
1027 recovery of the model in the corresponding cells. In our case we computed the  
1028 sensitivity kernels in an area of 16 km x 18 km around the crater. We divided  
1029 this area into 1152 cells with  $\Delta S = 0.25 \text{ km}^2$ . We used several time lag in the  
1030 coda waves with 20 s-long moving windows and 5 s of steep. Data are discarded  
1031 when corresponding  $CC$  is  $< 0.75$ . For periods  $P_1$ ,  $P_2$  and  $P_3$  we used 312, 284,  
1032 and 274 data respectively for the inversion. We did not consider topography in  
1033 this procedure.

### 1034 *Appendix A.3. Localization of structural changes*

1035 The structural changes in the medium can be localized by a similar ap-  
1036 proach as that used for velocity variations (Planès et al., 2014; Obermann et

1037 al., 2013). The data are the decorrelation ( $DC$ ) values that are obtained directly  
 1038 from the stretching method as:

$$DC = 1 - CC \tag{A.8}$$

1039 where  $CC$  are the correlation coefficients calculated between the stacked corre-  
 1040 lation functions of the current study period and those of the reference period  
 1041 (21 to 27 March 2014). To estimate the horizontal distribution of the decorre-  
 1042 lation  $DC(x_0)$ , we adapt the least-squares inversion described in the previous  
 1043 subsection (Equation A.5) to the decorrelation measurements:

$$1044$$

$$1045 d_i = DC_i ; G_{i,j} = \frac{c\Delta S}{2} K_{i,j} \text{ and } m_j = \sigma_j$$

1046

1047 where  $DC_i$  is the vector of the decorrelation values for each station pairs.  $G_{i,j}$   
 1048 is the matrix of the sensitivity kernels  $K_{i,j}$  for station pair  $i$  and cell  $j$ , weighted  
 1049 by the area of the cells  $\Delta S$  and the Rayleigh wave group velocity ( $c/2$ ).  $m$  is the  
 1050 vector of the scattering cross-section density changes that we want to estimate  
 1051 at each cell  $j$ . The initial model  $m_0$  is again null everywhere and we used an  
 1052 iterative inverse procedure to constrain the values of  $m$  to be positive (Oberman  
 1053 et al., 2013). As for velocity changes, we used a 20 s-long moving windows with  
 1054 steps of 5 s, in the band 0.1 – 1 Hz. For  $P_1$ ,  $P_2$  and  $P_3$ , we used 175, 174 and  
 1055 201 observations respectively as data for the inversions.